METEOROLOGICAL EFFECTS ON THE ACCURACY OF THE MEASUREMENT OF RADAR CROSS SECTIONS

by

PAULA S. AQUI

S.B., Massachusetts Institute of Technology
(1989)

SUBMITTED IN PARTIAL FULFILLMENT OF
THE REQUIREMENTS FOR THE
DEGREE OF

MASTER OF SCIENCE IN
AERONAUTICS AND ASTRONAUTICS

at the

MASSACHUSETTS INSTITUTE OF TECHNOLOGY
February 1991

Signature of Author _____
Department of Aeronautics and Astronautics
February 1991

Certified by _____
Associate Professor R. John Hansman
Department of Aeronautics and Astronautics
Thesis Supervisor

Accepted by _____
Professor Harold Y. Wachman
Chairman, Department Graduate Committee

Meteorological Effects on the Accuracy of the Measurement of Radar Cross Sections

by
Paula S. Aqui

Submitted to the Department of Aeronautics and Astronautics
in partial fulfillment of the requirements for the Degree of
Master of Science

Abstract

A method of determining the attenuation of radar signals due to precipitation was developed, in order to make appropriate corrections to radar cross section measurements based on radar reflectivity measurements. Previous work was reviewed, and used as a basis for the proposed algorithm, the validity of which was tested using data from experiments conducted at the Kiernan Reentry Measurements Site on the Kwajalein Atoll in the Marshall Islands. Scanning procedures and timing issues were also addressed. The relevant time scales were determined from an analysis of periodic weather scans made in the South Pacific. These Plan Position Indicator scans were made at five minute intervals at an elevation of 1.2° and out to a range of 120 km by NASA for their Tropical Rainfall Measurement Mission. The algorithm was also applied to the problem of defining meaningful criteria for aborting missions due to weather, and the results were presented in a graphical format.

Thesis Supervisor: Dr. R. John Hansman
Associate Professor of Aeronautics and Astronautics

Acknowledgements

This work was supported by the MIT Lincoln Laboratory under contract BX-3066. The author would like to thank David Makofski and David Wolff of the NASA Goddard Space Flight Center, for all their assistance in making the NASA TRMM data available. The author would also like to thank Dennis Hall of MIT Lincoln Laboratory for much support and help, as well as Amy Gardner and Amy Prichett for their work on data reduction. The author would especially like to thank Craig Wanke for his continuing support, advice, and tolerance throughout this project.

Contents

List of Tables

List of Figures

1. Introduction

Various meteorological phenomena (clouds, rain, etc.) cause attenuation of radar signals, thereby producing errors in precision radar cross section (RCS) measurements. This problem has become increasingly acute as more precise, and higher frequency radars, which are attenuated more strongly, are developed. Much work has been done to quantify the attenuation due to atmospheric gases, clouds, and precipitation, and several expressions for attenuation in terms of some measurable quantity, such as radar reflectivity or rainfall rate, have been proposed. However, little has been done toward a practical application of these relations.

This effort was undertaken in an attempt to formulate an algorithm which corrects for the attenuation of RCS measurements due to weather, and which can be executed directly from weather scans. Two specific wavelengths, 0.86 cm and 5.3 cm, were considered in the development of the algorithm, for which experimental data was available from the Kiernan Reentry Measurements Site (KREMS) located on the Kwajalein Atoll in the Marshall Islands.

The associated issues of timing and scanning strategies have been addressed, since some minimum number of weather scans must be made within a reasonable time of the target track. In order to quantify this, typical time scales at the KREMS facility have been established by an analysis of periodic weather scans of the area. These plan-position indicator (PPI) scans were taken at five minute intervals at an elevation of 1.2°, and were made by NASA in support of the Tropical Rainfall Measurement Mission (TRMM). Factors affecting the actual application of the algorithm, such as identification of the freezing level in clouds and inaccuracies in radar measurements of the weather, were also discussed, as well as the possibility of establishing meaningful criteria for aborting RCS measurement missions.

Chapter 2 outlines the motivation behind the project, including a description of the KREMS facility, upon which this work has been focused. Chapter 3 details the relevant analytic and empirical formulations which have previously been developed, and which form the basis for the proposed algorithm. Experimental validation of the algorithm is presented in Chapter 4, and implementation issues are addressed in Chapter 5. The results of the project are summarized in Chapter 6.

2. Background

There is a growing impetus for the use of higher frequency radars because of their small size, and greater sensitivity. Radar systems are also becoming more accurate as technology improves, and the requirement for more precise RCS measurements increases. The accuracy of these measurements however, is affected by the presence of hydrometeors, in the form of clouds or precipitation, in the path of the radar signal.

This problem has been equally troubling at the KREMS radar facility, which is situated on the Kwajalein Atoll in the Marshall Islands at 9°N latitude and 167°E longitude. Field tests there have often been aborted due to weather in the area, restricting the usefulness and productivity of the facility. This project was undertaken in an attempt to reduce the problem, with particular emphasis on the C- and K_a-band radars at KREMS. An outline of the facility and its radars is given below, followed by.a description of the MOIST programs, which were developed in an endeavour to quantify the problem there.

2.1. The KREMS Radar Facility

The KREMS facility operates several radars, which may be used either for target tracking, or for weather scans. The Target Resolution and Discrimination Experiment (TRADEX) radar operates at L- and S-bands, and the ARPA (Advanced Research Projects Agency) Long-Range Tracking and Instrumentation Radar (ALTAIR) operates at UHF and VHF. The ARPA Lincoln C-band Observables Radar (ALCOR) operates at C-band, and was later modified to include K_a- and W-band, operation. The location of these radar systems in the Kwajalein Atoll is shown in Figure 2.1.

This work has been centered on the ALCOR C-band (5.7 GHz) and the K_a-band, or millimeter wave (MMW 35 GHz), radar systems situated at the KREMS field site on

Roi-Namur (Figure 2.2), at the northeastern corner of the Kwajalein Atoll. Both radars are capable of target-tracking and weather scans.

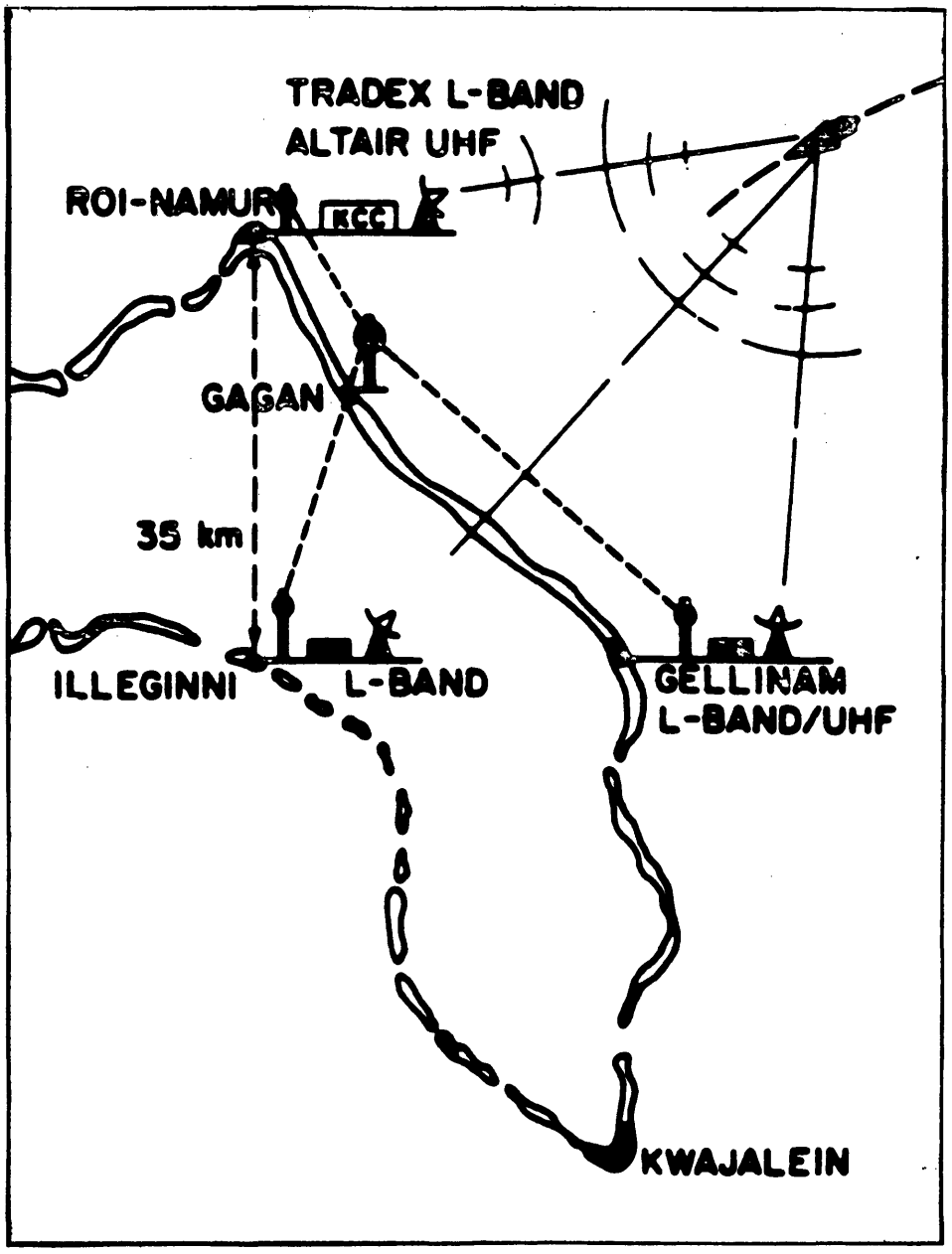

Figure 2.1 Location of the radar systems in the Kwajalein Atoll.

The facility originated out of a need for a better understanding of the physical effects of the atmosphere upon reentry vehicles, based on both theoretical work and experiments. The scope and objectives of their program has changed over the years however, with primary interest shifting to the problem of object recognition. Various field tests are executed at the facility utilizing reentry vehicles, calibration spheres, and satellites, which are tracked by the various radars. Unfortunately, these tests are often contaminated, or need to be postponed due to clouds or precipitation in the area.

2.2. The MOIST Programs

Previous efforts have been made at the KREMS facility to counteract the weather attenuation problem. In particular, a series of programs called MOIST I and MOIST II were developed in an attempt to quantify the severity of existing weather from range scan measurements. However, these programs were not designed to make corrections to RCS measurements. Radar scans of the weather measure the effective reflectivity factor, Z_e, (as defined in section 3.2), and range scans in particular measure the Z_e levels of successive range cells at a particular azimuth and elevation, and out past the weather of interest.

There are two methods for recording range scans at the KREMS facility. Radar measurements of the weather can be recorded digitally, or sent to a video recording system where the Z_e levels are represented by different colours, in range-height indicator (RHI) or plan-position indicator (PPI) format. RHI scans display Z_e levels of weather cells along a particular azimuth, in terms of altitude versus ground range, and an example for ALCOR is shown in Figure 2.2. On the other hand, PPI scans display the Z_e levels of weather cells at a particular elevation, and out to a particular range, and may encompass the full 360° range of azimuth settings. A typical PPI scan for ALCOR is also shown in Figure 2.2.

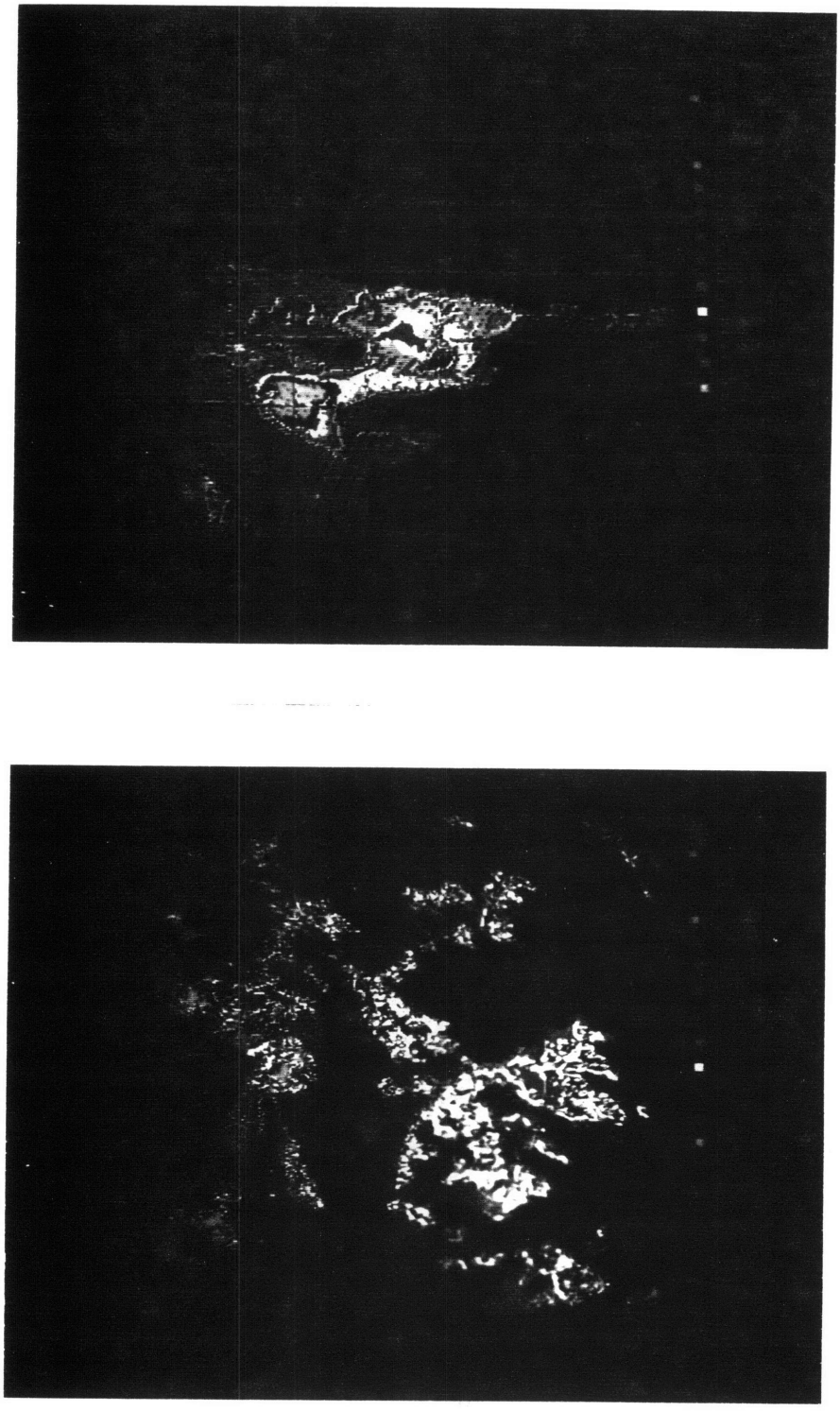

Figure 2.2 Typical RHI scan (top) and PPI scan (bottom) made by ALCOR.

Digitally recorded range scans are used by the MOIST I program to calculate the moisture content (liquid water content), M, and a parameter called the Environmental Severity Index, ESI, of the range cells. The liquid water content is calculated from the measured Z_e values using relationships of the form $M = a (Z_e)^b$, as shown in Table 2.1. These relationships were developed for KREMS by the Air Force Geophysical Laboratory (AFGL), from correlation runs performed at the Kwajalein Atoll during convective precipitating weather conditions (which is typical of the type of rainfall in the region).

Altitude Range (km)	Predominant Species	M (gm m^{-3})
20 to 10	Ice (Cirrus)	$0.045\ Z_e^{0.460}$
10 to 7.8	Small snow	$0.043\ Z_e^{0.523}$
7.8 to 4.6	Large snow	$0.025\ Z_e^{0.390}$
4.6 to 0	Rain	$0.0055\ Z_e^{0.565}$

SOURCE: Pearson (December 1985).

Table 2.1 M-Z_e relations used in the MOIST programs.

The Environmental Severity Index, ESI in gm km^2 gm^{-3}, is a function of the liquid water content, M in gm m^{-3}, and is defined as

$$ESI = \int_{h_1}^{h_2} (M\,h)\,dh \qquad (2.1)$$

where h = altitude of target or range bin in km,

h_2 = top of cloud layer,

and h_1 = bottom of cloud layer.

This parameter was intended as an indication of weather severity, particularly for field tests involving reentry vehicles. It is a weighted measure of the total moisture content in the signal path, with the altitude weighting being used in recognition of greater velocities of reentry vehicles at higher altitudes. An ESI < 1 is considered "good weather", while an ESI > 5 is considered "foul weather". Unfortunately, this particular measure of weather severity was found to be sensitive to rapid changes in liquid water content, and difficult to interpret physically.

As a result, the MOIST II program was proposed, in which parameters with greater physical significance are calculated. These parameters are the Vertical Moisture Pressure, VMP in gm m^{-2}, and the Trajectory Moisture Pressure, TMP in gm m^{-2}, and are defined as

$$VMP = \int_{h_1}^{h_2} M \, dh \tag{2.2}$$

and

$$TMP = \int_{s_1}^{s_2} M \, ds \tag{2.3}$$

where s = range of target or range bin in km,

s_2 = range to top of cloud layer,

and s_1 = range to bottom of cloud layer.

The VMP is a measure of the total moisture mass in a 1 m^2 column above the vehicle altitude, and the TMP is a measure of the total moisture mass through which the vehicle has traversed. It should be noted that these parameters have their intended meaning only if they are calculated during a target track, while the ESI has some significance for range scans as well as target tracks. It is unclear whether the MOIST II parameters were ever intended to be used in range scan measurements, but when used in such scans they measure the moisture pressure in the path of the radar signal instead. Unfortunately, these

parameters only quantified the effects of hydrometeor impingement on reentry vehicles, and the problem of attenuated RCS measurements was not addressed, which is instead the purpose of this work.

3. Proposed Correction Algorithm

The proposed algorithm was developed to make corrections to RCS measurements of targets being tracked by radar, and these corrections are based on radar-measured intensity levels of weather between the radar and the target. Weather intensity is usually measured in terms of a parameter known as the reflectivity factor, Z , which is typically given in units of dBZ (Z being measured in $mm^6 m^{-3}$), as defined in section 3.2. Electromagnetic waves travelling through the air are also attenuated by atmospheric gases (as described in Appendix A), but this can be readily accounted for during the calibration of any radar system.

This project also does not attempt to deal with frozen forms of precipitation, such as snow or hail, which are not present in the vicinity of the KREMS facility. However even in the south Pacific, clouds may contain ice or small snow particles at high altitudes, as well as water droplets. Fortunately, for centimeter and millimeter waves like ALCOR and MMW, the attenuation due to ice clouds is significantly less than that due to water clouds, as can be seen from the calculations made by Gunn and East (1954), for attenuation values of ice and water clouds, listed in Appendix B. Therefore, attenuation due to ice particles in clouds will be neglected in the calculations.

The algorithm calculates the total two-way attenuation along the path of a radar signal from the intensity levels of the weather cells in that path, as outlined in Figure 3.1. Two possible relations to convert the intensity level of each weather cell to an equivalent rainfall rate (R in mm hr^{-1}) were employed. One was an empirical relation, and the other Z-R relation was an analytic expression, but based on empirical observations of droplet-size distributions for stratiform rain. Once the rainfall rates for the weather cells have been calculated, their two-way attenuation rates (k_2 in dB km^{-1}) could be determined, for which two possible k-R relations were also used. Finally, the attenuation rates were multiplied by

the cell depths to get the two-way attenuation values for the cells, and then summed to get the total two-way attenuation along the path of the radar signal. It was found to be necessary to include the temperature of the hydrometeors and the location of the freezing level, in order to accurately calculate the attenuation rates.

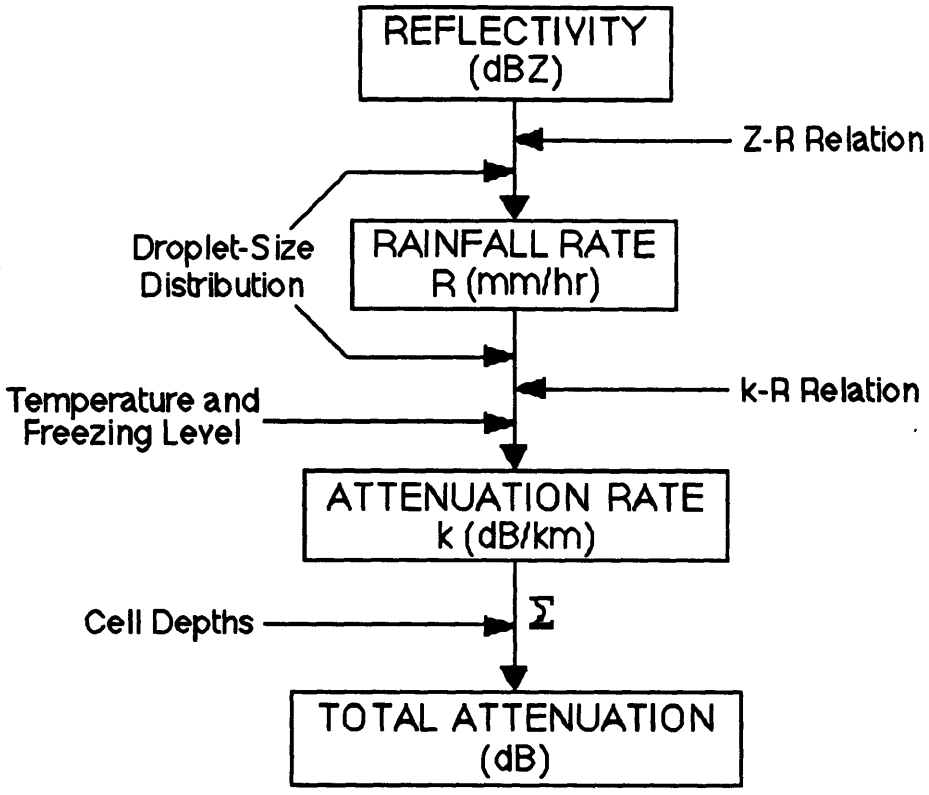

Figure 3.1 Structure of the attenuation algorithm.

The various components of this algorithm are presented in further detail in the following sections, beginning with a description of attenuation of electromagnetic waves by hydrometeors. This is followed by an outline of the radar equation and its relationship to the reflectivity factor. Then, the two Z-R relations used in the algorithm are presented, as are the two possible k-R relations.

3.1. Scattering and Attenuation

An electromagnetic wave incident on a water or ice particle sets up oscillating magnetic and electric dipoles within the droplet, which removes energy from the incident field. Some of this energy is re-radiated (scattered) at the incident frequency, while the rest is absorbed as heat. The total effect is an attenuation of the incident wave, which, in this paper, is assumed to be planar. The amount of attenuation depends on the size of the hydrometeor, as well as its shape.

Some work has been done to quantify the attenuation due to non-spherical particles, and Battan (1973) found that randomly oriented oblate and prolate spheroids caused greater attenuation, of plane polarized electromagnetic radiation, than spheres of the same volume. However, the increase in attenuation became significant only for large deviations from the spherical shape (axis ratios greater than about 1: 2). For most water droplets in clouds and rain, the surface tension of the drop is strong enough to maintain an essentially spherical shape. Large raindrops do tend to be oblate, but the number of these large drops is a small fraction of the number of small, spherical drops. Therefore, the assumption will be made that all of the drops are spherical, since this would be quite adequate for a calculation of the total attenuation caused by these drops.

A theory for the scattering of plane waves by spherical particles was first developed by Mie (1908). This theory developed analytical expressions for various attenuation cross-sections. The scattering cross-section, Q_s, is defined as that area which, when multiplied by the incident intensity, gives the power scattered by the particle, and the absorption cross-section, Q_a, is defined as that area which, when multiplied by the incident intensity, gives the power absorbed by the particle. The total attenuation cross-section, Q_t, is the sum of Q_s and Q_a , and is defined as the area which, when multiplied by the incident

intensity, gives the total power removed from the incident electromagnetic wave. For a spherical particle, these cross-sections can be expressed as follows.

$$Q_s = \frac{\lambda^2}{2\pi} \sum_{n=1}^{\infty} (2n + 1)\left(|a_n|^2 + |b_n|^2\right) \tag{3.1}$$

and

$$Q_a = Q_t - Q_s \tag{3.2}$$

with

$$Q_t = \frac{\lambda^2}{2\pi}(-\mathrm{Re})\sum_{n=1}^{\infty} (2n + 1)(a_n + b_n) \tag{3.3}$$

where λ = wavelength of incident wave,

a_n = coefficient of nth magnetic mode,

and b_n = coefficient of nth electric mode.

The coefficients a_n and b_n are made up of nth order Spherical Bessel functions, whose arguments are the complex index of refraction for the particle, and the dimensionless variable α, which is defined as

$$\alpha \equiv \frac{\pi D}{\lambda} \tag{3.4}$$

where D = the diameter of the sphere.

For small hydrometeors, whose diameters are small compared with the wavelength, $\alpha \ll 1$, and terms of higher order than the sixth power of α may be neglected from the Mie equations. The resulting expressions are known as the Rayleigh approximations for the scattering and absorption cross-sections.

$$Q_s = \frac{2\lambda^2 \alpha^6 |K|^2}{3\pi} \tag{3.5}$$

and

$$Q_a = \frac{\lambda^2 \alpha^3 \, \mathrm{Im}(-K)}{\pi} \tag{3.6}$$

where

$$K \equiv \frac{m^2 - 1}{m^2 + 2} \tag{3.7}$$

m being the complex index of refraction for water. Note that for $\alpha \ll 1$, $Q_s \ll Q_a$ so that the total attenuation cross-section may be approximated by the absorption cross-section alone, $Q_t \approx Q_a$. However, for larger particles both Q_s and Q_a must be calculated.

The amount of attenuation due to a collection of hydrometeors can be calculated from their total attenuation cross-sections, by summing over all the particles in the path of the electromagnetic wave. The one-way attenuation rate, k, in units of dB km^{-1} is given by

$$k = 0.4343 \sum_{vol} Q_t \tag{3.8}$$

where Q_t is measured in units of square centimeters and the summation is made over 1 m^3.

3.2. The Radar Equation, Reflectivity, and Reflectivity Factor

The average power of a radar signal, reflected off a group of hydrometeors, and received by the radar, $\overline{P}_r$, is given by

$$\overline{P}_r = \frac{P_t A_e h}{8 \pi r^2} \sum_{vol} \sigma \tag{3.9}$$

where P_t = transmitted power,

A_e = equivalent antenna aperture,

h = length of pulse in space,

r = range of hydrometeors,

and $\sum_{vol} \sigma$ = the total back-scatter cross-section of the hydrometeors in a unit volume, also known as "the reflectivity".

The back-scatter cross-section, σ, is defined as that area which, when multiplied by the incident intensity, gives the total power radiated by an isotropic source which would radiate the same power in the backward direction as the scatterer. The Mie expression for the back-scatter cross-section of a spherical particle is

$$\sigma = \frac{\lambda^2}{4\pi}\left|\sum_{n=1}^{\infty} (-1)^n (2n+1)(a_n - b_n)\right|^2 \tag{3.10}$$

and for $\alpha \ll 1$, the Rayleigh approximation is

$$\sigma = \frac{\lambda^2 \alpha^6 |K|^2}{\pi} = \frac{\pi^5 |K|^2}{\lambda^4} D^6 \tag{3.11}$$

When the Rayleigh approximation is valid, the received power can be used to measure the reflectivity factor, Z in $mm^6\ m^{-3}$, of the particle which is defined as

$$Z \equiv \sum_{vol} D^6 \tag{3.12}$$

This may be done by using the above definition of Z together with equations (3.9) and (3.11), resulting in the relation

$$\overline{P}_r = \frac{P_t A_e h \pi^4 |K|^2}{8 r^2 \lambda^4} Z \tag{3.13}$$

When Rayleigh scattering does not apply, equation (3.13) can no longer be used to calculate Z, but instead determines the 'effective radar reflectivity factor', Z_e, which can be defined by the equation

$$Z_e \equiv \frac{\lambda^4}{\pi^5 |K|^2} \sum_{vol} \sigma \tag{3.14}$$

For a collection of particles throughout a volume, such as in a cloud or a region of rainfall, the particle-size distribution must be known in order to calculate either the reflectivity or the reflectivity factor. If the particle-size distribution is expressed in terms of N, the number of drops of diameter D per unit volume over a discrete interval of diameters ΔD, then the reflectivity is

$$\sum_{vol} \sigma = \sum_{i} N_i \sigma_i \Delta D_i \tag{3.15}$$

and similarly, the reflectivity factor is

$$Z = \sum_{i} N_i D_i^6 \Delta D_i \tag{3.16}$$

3.3. Droplet-Size Distributions

In order to develop an analytic expression for the reflectivity factor, Z, as a function of rainfall rate, R, it is necessary to assume some distribution of droplet sizes. One of the Z-R relations used in the algorithm was analytic in nature, and based on an expression for the droplet-size distribution in stratiform rain, proposed by Marshall and Palmer (1948). This expression was also used in the development of both the k-R relations used in the algorithm, and it was expressed in terms of N_D, the number of drops of diameter D per unit volume, in units of cm^{-4}, as a function of D in cm, Λ in cm^{-1} and N_o in cm^{-4}, as follows.

$$N_D = N_o e^{-\Lambda D} \tag{3.17}$$

with $N_o = 0.08$ and $\Lambda = 41\ R^{-0.21}$, and where R is the rainfall rate in mm hr^{-1}. This expression was derived as a fit to droplet-size distribution observations made in Ottawa

(see Figure 3.2), and similar data from Laws and Parson (1943) for rain over Washington, DC. It is widely accepted as being valid for most occurrences of stratiform rain.

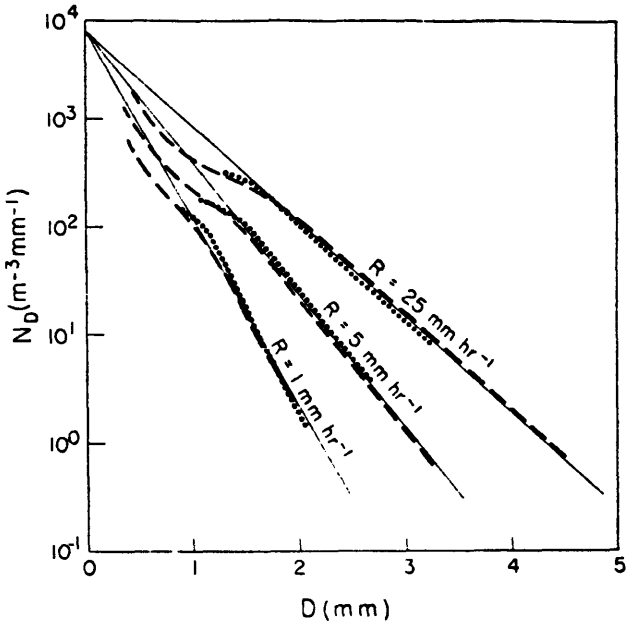

Figure 3.2 Distribution function (solid straight lines) compared with results of Laws and Parsons (broken lines) and Ottawa observations (dotted lines). From Marshall and Palmer (1948).

Wexler and Atlas (1963) later modified the Marshall-Palmer (M-P) expression of equation (3.17), in order to achieve a better fit to the data at small drop sizes. This was accomplished by using:

$$\text{at } R = 1 \text{ mm hr}^{-1} \qquad N_o = 0.01 \text{ cm}^{-4} \qquad \text{and} \qquad \Lambda = \begin{cases} 41\, R^{-0.21} & \text{for } D > 1 \text{ mm} \\ 20 & \text{for } D \le 1 \text{ mm} \end{cases}$$

$$\text{at } R = 5 \text{ mm hr}^{-1} \qquad N_o = 0.01 \text{ cm}^{-4} \qquad \text{and} \qquad \Lambda = \begin{cases} 41\, R^{-0.21} & \text{for } D > 1.5 \text{ mm} \\ 15 & \text{for } D \le 1.5 \text{ mm} \end{cases}$$

3.4. The Z-R Relations

As mentioned earlier, two different relations for converting reflectivity factor, Z, to rainfall rate, R, were tested for use in the algorithm. The first was developed by Wexler and Atlas (1963) using the modified M-P droplet-size distribution, and the Mie scattering cross-sections calculated by Herman *et al* (1961) for wavelengths of 0.62, 0.86, 1.24, 1.87, 3.21, 4.67, 5.5 and 10.0 cm at 0°C. Equation (3.15) was expanded to the form

$$\sum_{vol} \sigma = \frac{N_o \lambda^3}{4 \pi^2} \sum_i S_i \alpha_i^2 e^{-\Lambda D_i} \Delta\alpha_i \qquad (3.18)$$

where S_i was defined as the ratio of the back-scatter to the geometric cross-section, or the normalized back-scatter cross-section, of the particle. This, together with equation (3.14), produced a relation between rainfall rate and effective reflectivity factor. In other words, a Z_e-R relation (for Mie scattering) as follows.

$$Z_e = \frac{N_o \lambda^7}{4 \pi^7 |K|^2} \sum_i S_i \alpha_i^2 \exp\left(\frac{-41\lambda\alpha_i}{\pi} R^{-0.21}\right) \Delta\alpha_i \qquad (3.19)$$

The normalized cross-sections calculated by Herman *et al* (1961) were presented in terms of α_i, with $\Delta\alpha_i = 0.1$ for wavelengths from 0.62 cm to 1.87 cm, and $\Delta\alpha_i = 0.02$ for 3.2 cm to 10 cm.

Wexler and Atlas tabulated these Z_e-R relations, together with similar relations for distributions proposed by Mueller and Jones (1960), and for the results of Gunn and East (1954) (with Haddock's calculations and the Laws and Parsons drop-size distributions). These are shown in Table 3.1 below. The modified M-P distributions were not included in the table, but were said to "...have a coefficient about 30 per cent higher than the straight M-P distribution with the same exponent of R."

Wavelength (cm)	R interval (mm hr^{-1})	Z (mm^6 m^{-3}) at 0°C		
		M-P	Gunn & East*	Mueller-Jones
0.62	0 - 5	240 $R^{1.10}$		450 R
	5 - 20	345 $R^{0.90}$		
	20 - 100	540 $R^{0.75}$		
0.86	0 - 5	350 $R^{1.32}$		950 R
	5 - 20	450 $R^{1.15}$		
	20 - 100	780 $R^{0.95}$		
1.24	0 - 5	356 $R^{1.50}$		1280 R
	5 - 20	460 $R^{1.35}$		
	20 - 100	820 $R^{1.15}$		
1.87	0 -20	330 $R^{1.54}$		1150 R
	20 - 50	500 $R^{1.40}$		
	50 - 100	750 $R^{1.30}$		
3.21		275 $R^{1.55}$	310 $R^{1.56}$	890 R
4.67		280 $R^{1.45}$		860 R
5.5		280 $R^{1.45}$		860 R
5.7			210 $R^{1.60}$	
10.0		295 $R^{1.45}$	210 $R^{1.60}$	810 R

* Values calculated at 18°C.
SOURCE: Wexler and Atlas (1963).

Table 3.1 Wexler and Atlas (1963) Z-R relations corrected for Mie scattering.

For MMW ($\lambda = 0.86$ cm), the straight M-P relation was taken directly from the M-P column of Table 3.1, while the corresponding value for ALCOR ($\lambda = 5.3$ cm) was derived by interpolation. The coefficients of the straight M-P relations were then increased

by 30% to get the Z-R relations based on the modified M-P distributions, and the resulting expressions, for ALCOR and MMW respectively, were

$$Z = 364\, R^{1.45} \tag{3.20}$$

and

$$Z = \begin{cases} 455\, R^{1.32} & \text{for } 0 \le R \le 5 \text{ mm hr}^{-1} \quad (3.21a) \\ 585\, R^{1.15} & \text{for } 5 \le R \le 20 \text{ mm hr}^{-1} \quad (3.21b) \\ 1014\, R^{0.95} & \text{for } 20 \le R \le 100 \text{ mm hr}^{-1} \quad (3.21c) \end{cases}$$

These relations were then inverted to express R as a function of Z, for both ALCOR and MMW respectively, as follows.

$$R = 0.0171\, Z^{0.69} \tag{3.22}$$

and

$$R = \begin{cases} 0.00969\, Z^{0.758} & \text{for } Z \le 35.8 \text{ dBZ} \quad (3.23a) \\ 0.00392\, Z^{0.870} & \text{for } 35.8 \le Z \le 42.5 \text{ dBZ} \quad (3.23b) \\ 6.85\times10^{-4}\, Z^{1.05} & \text{for } Z \ge 42.5 \text{ dBZ} \quad (3.23c) \end{cases}$$

The second Z-R relation tried in the algorithm was an expression based directly on empirical data, which was suggested by Blanchard (1953) for non-orographic rain over Hawaii, and which is expressed as follows.

$$Z = 290\, R^{1.41} \tag{3.24}$$

which implies

$$R = 0.0179\, Z^{0.709} \tag{3.25}$$

There have actually been a great number of empirical Z-R relations presented over the years. In fact, Battan (1973) lists 69 different relations for various types of rainfall at many locations throughout the world. However, Blanchard's relation was chosen because

it was most appropriate for the KREMS facility in the South Pacific, where most of the rainfall of concern is convective in nature.

3.5. The k-R Relations

In order to derive the one-way attenuation rate, k in dB km^{-1}, from the rainfall rate, R, two possible sets of k-R relations were evaluated. One was developed by Waldteufel (1973) for the M-P drop-size distribution at 18°C, while the other was developed by Wexler and Atlas (1963) for their modified M-P drop-size distributions at 0°C. Both sets of relations were calculated from the full Mie scattering cross-sections, and are given in detail in the following sections.

3.5.1. The Waldteufel k-R Relations

The Waldteufel k-R relations for ALCOR and MMW were derived by estimating a straight-line best fit to his plots of attenuation rate versus rainfall rate shown in Figure 3.3. This was done at 5.7 GHz and 35 GHz for ALCOR and MMW respectively. The resulting two-way attenuation rate, k_2 in dB km^{-1}, for ALCOR and MMW at 18°C was

$$k_{2A} = \begin{cases} 4.00\times10^{-3}\, R^{1.01} & \text{for } 0 \le R \le 2 \text{ mm hr}^{-1} \quad (3.26a) \\ 3.62\times10^{-3}\, R^{1.15} & \text{for } 2 \le R \le 10 \text{ mm hr}^{-1} \quad (3.26b) \\ 2.46\times10^{-3}\, R^{1.32} & \text{for } 10 \le R \le 200 \text{ mm hr}^{-1} \quad (3.26c) \end{cases}$$

and

$$k_{2M} = \begin{cases} 0.460\, R^{1.09} & \text{for } 0 \le R \le 5 \text{ mm hr}^{-1} \quad (3.27a) \\ 0.566\, R^{0.96} & \text{for } 5 \le R \le 20 \text{ mm hr}^{-1} \quad (3.27b) \\ 0.660\, R^{0.97} & \text{for } 20 \le R \le 200 \text{ mm hr}^{-1} \quad (3.27c) \end{cases}$$

respectively, for k_{2A} and k_{2M} in dB km^{-1} and R in mm hr^{1}.

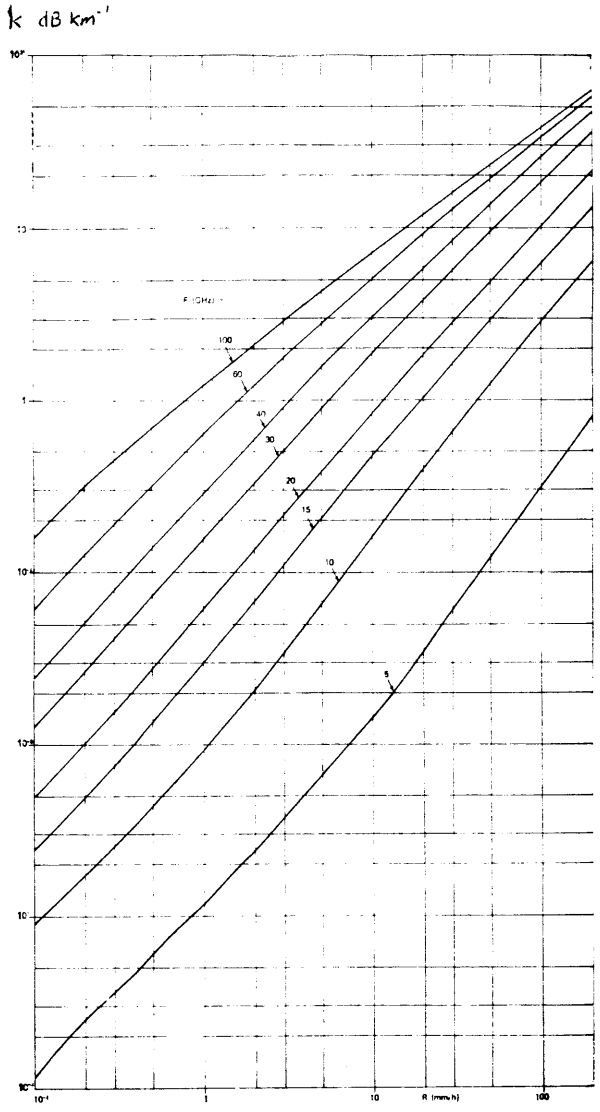

Figure 3.3 Attenuation rate k as a function of R for different values of frequency, for the Marshall-Palmer distribution. T = 18°C. From Waldteufel (1973).

Waldteufel also investigated the effects of temperature on attenuation rate, tabulating his results for several frequencies and for three values of rainfall rate. This table is shown in Appendix C. Resulting plots of one-way attenuation rate versus rainfall rate for 5 GHz and 30 GHz are shown in Figure 3.4.

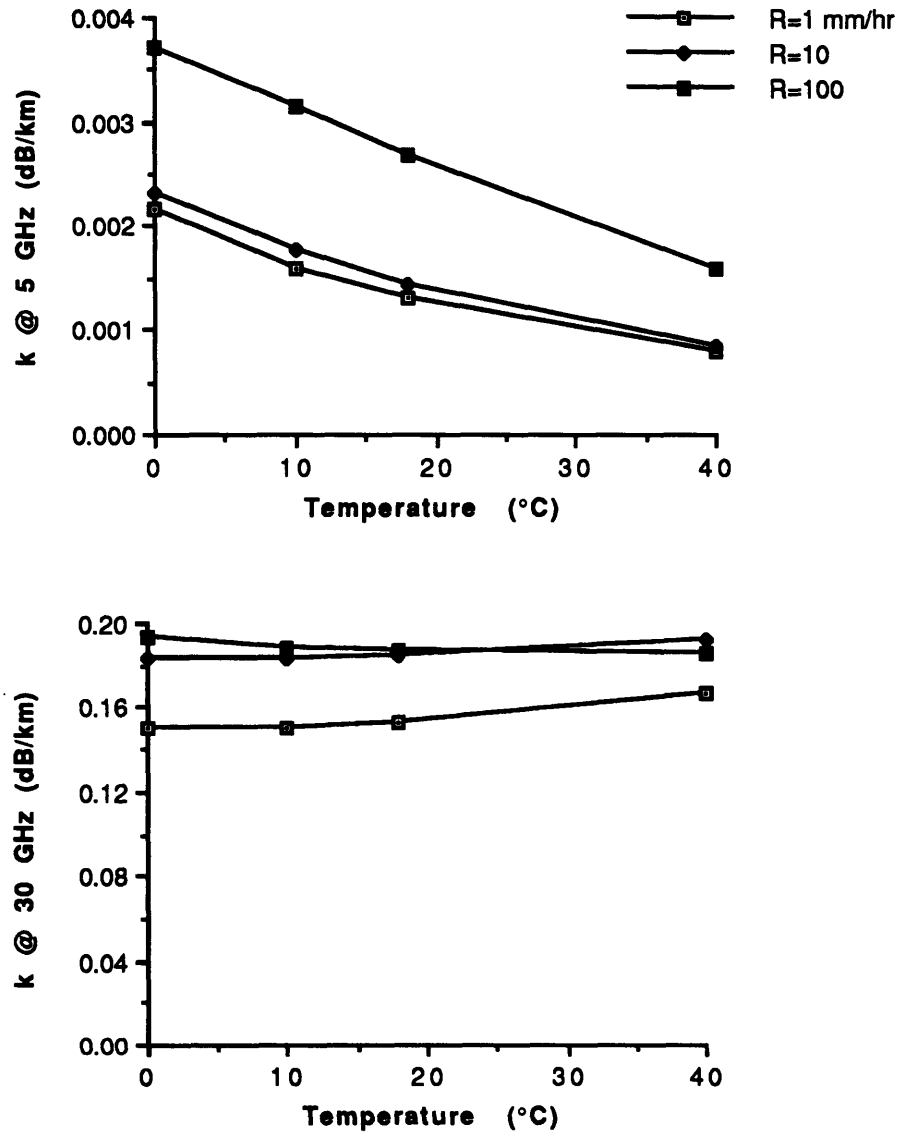

Figure 3.4 Effects of temperature on k, the one-way attenuation rate, at 5 GHz and 30 GHz for three rainfall rates, as calculated by Waldteufel (1973).

For frequencies above about 35 GHz the attenuation rate was found to be relatively independent of temperature in the range of 0 to 40°C, varying by no more than 5%. Lhermitte (1990a) obtained similar results for frequencies of 35 GHz and higher. Also, between approximately 18 GHz and 35 GHz, Waldteufel's values were within 10% over the range of temperatures, except at very low rain rates. Hence, the attenuation rate for

MMW was assumed to be independent of temperature, so that equations (3.27) were sufficiently general. For frequencies below about 18 GHz however, as is the case for ALCOR, there was considerable variation in the attenuation rate with temperature. This is not surprising, since at such low frequencies most raindrops are within the Rayleigh scattering range, where the attenuation is proportional to the Im(-K), which varies with temperature.

Consequently, for ALCOR the variation of attenuation rate with temperature can be determined directly from the Im(-K) values at that wavelength (5.3 cm). These Im(-K) values were derived, for various temperatures, from calculations by Waldteufel (1973), and the expression for the complex index of refraction developed by Lane and Saxton (1952). Details of the derivation are given in Appendix D. These values were plotted versus temperature, and a quadratic curve fit to the data was done (see Figure 3.5).

The curve fit resulted in the following expression for Im(-K) as a function of temperature, T, in °C:

$$\text{Im}(-K) = 2.03\times10^{-2} - 6.26\times10^{-4}\,T + 8.46\times10^{-6}\,T^2 \qquad (3.28)$$

Then since the two-way attenuation rate at 18°C was known, the coefficients of the Im(-K) function were multiplied accordingly to produce the temperature-dependent function for the two-way attenuation rate for ALCOR, k_{2A} in dB km^{-1}.

$$k_{2A} = \begin{cases} (6.89\times10^{-3} - 2.12\times10^{-4}T + 2.87\times10^{-6}T^2)\,R^{1.01} & \text{for } 0 \le R \le 2 \text{ mm hr}^{-1} \quad (3.29a) \\ (6.24\times10^{-3} - 1.92\times10^{-4}T + 2.60\times10^{-6}T^2)\,R^{1.15} & \text{for } 2 \le R \le 10 \text{ mm hr}^{-1} \quad (3.29b) \\ (4.24\times10^{-3} - 1.31\times10^{-4}T + 1.76\times10^{-6}T^2)\,R^{1.32} & \text{for } 10 \le R \le 200 \text{ mm hr}^{-1} \quad (3.29c) \end{cases}$$

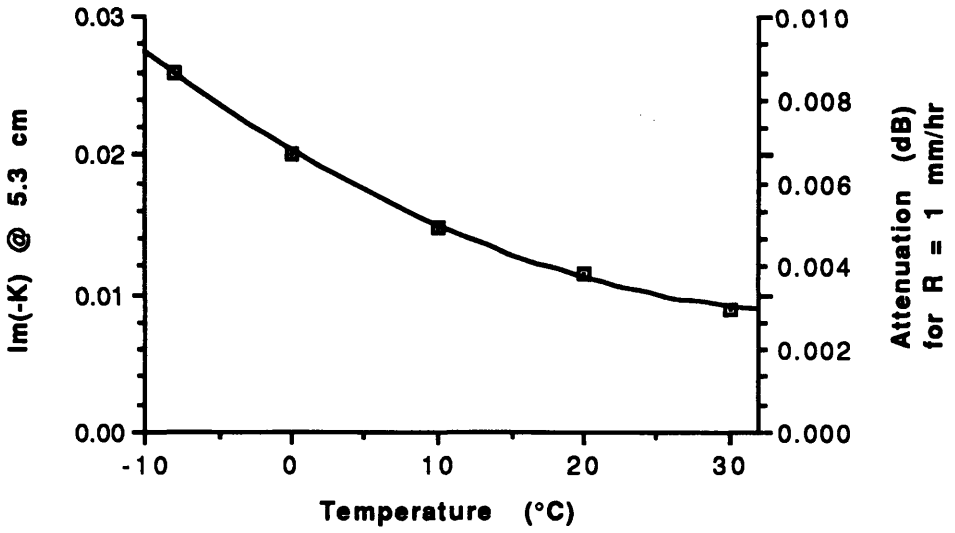

Figure 3.5 Quadratic curve fit to Im(-K) values, and attenuation values (for R = 1 mm hr^{-1}), for a wavelength of 5.3 cm, and for various temperatures.

3.5.2. The Wexler and Atlas k-R Relations

Wexler and Atlas also developed expressions of attenuation rate per unit rainfall rate versus rainfall rate, based on the data in Herman *et al* (1961). This was done for both the straight and modified M-P droplet-size distributions, as well as the Mueller-Jones (1960) distributions. These expressions, as well as those developed by Gunn and East (1954), are shown in Table 3.3.

The Wexler and Atlas values for the attenuation rates were taken from the modified M-P values. For ALCOR, the two-way attenuation rate at 0°C was found (by interpolation) to be

$$k_{2A} = 0.0072\,R \tag{3.30}$$

while the value for MMW was

$$k_{2M} = 0.62\,R \tag{3.31}$$

for k_{2A} and k_{2M} in dB km^{-1} and R in mm hr^{-1}. The coefficients of the Im(-K) function of equation (3.28) were then factored once again to produce the following expression for the two-way attenuation rate for ALCOR as a function of temperature.

$$k_{2A} = (0.0072 - 2.2\text{x}10^{-4}\,T + 3.0\text{x}10^{-6}\,T^2)\,R \tag{3.32}$$

Wavelength (cm)	M-P	Modified M-P	Mueller-Jones	Gunn and East*
0.62	0.50 - 0.37	0.52	0.66	
0.86	0.27	0.31	0.39	
1.24	$0.117\,R^{0.07}$	$0.13\,R^{0.07}$	0.18	$0.12\,R^{0.05}$
1.8				$0.045\,R^{0.11}$
1.87	$0.045\,R^{0.10}$	$0.050\,R^{0.10}$	0.065	
3.21	$0.011\,R^{0.15}$	$0.013\,R^{0.15}$	0.018	$0.0074\,R^{0.31}$
4.67	0.007 - 0.005	0.0053	0.0058	
5.5	0.004 - 0.003	0.0031	0.0033	
5.7				$0.0022\,R^{0.17}$
10	0.0009 - 0.0007	0.00082	0.00092	0.0003

* Values calculated at 18°C.
SOURCE: Wexler and Atlas (1963).

Table 3.3 Attenuation k/R (dB km^{-1}/mm hr^{-1}) at 0°C calculated by Wexler and Atlas (1963) for several drop-size distributions.

3.5.3. The Temperature Model

The temperature of each range cell was estimated, based on its altitude, using the Kwajalein Reference Atmospheres (1979), which lists standardized annual and monthly tables of temperature versus altitude for the Kwajalein Atoll. There was very little difference between the listings for those months in which experiments #1 and #2 were run, and the annual listing. Therefore, the annual reference atmosphere was used to determine the range cell temperatures for both experiment #1 and #2. These temperature values were plotted on a graph versus altitude, and a quadratic curve fit was done to produce an analytic expression for the temperature as a function of altitude. The resulting expression for the temperature, T in °C, as a function of the altitude, h in km, was

$$T = 29.2 - 5.19\,h - 0.104\,h^2 \tag{3.33}$$

3.6. The Attenuation Algorithm

The previous sections demonstrated the development of the relations used in the various steps of the proposed weather attenuation algorithm. The steps of the resulting algorithm are outlined in Figure 3.6. This diagram displays the choice of the Blanchard, or the Wexler and Atlas Z-R relations, for converting the effective reflectivity factor levels of weather cells to equivalent rainfall rates.

Also shown is the choice of the Wexler and Atlas, or the Waldteufel k-R relations, for deriving the attenuation rates from the equivalent rainfall rates. The use of the M-P droplet-size distribution in the Waldteufel k-R relations, and the modified M-P droplet-size distribution in the Wexler and Atlas k-R, and Z-R, relations is also indicated, as is the final summation of the attenuation values for the range cells.

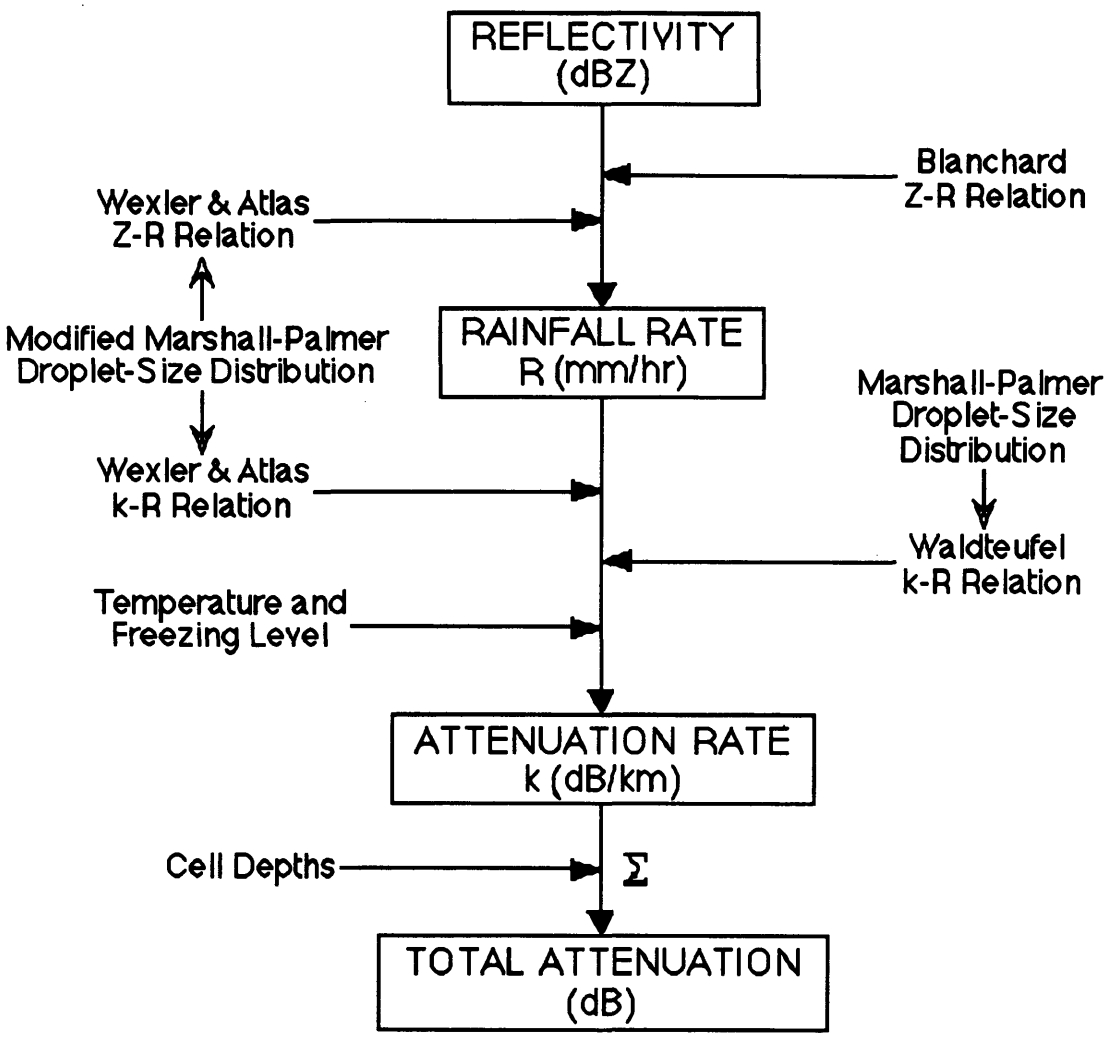

Figure 3.6 Structure of the proposed attenuation algorithm, with the optional Z-R and k-R relations.

4. Experimental Validation

As was mentioned in Chapter 2, there were two experiments carried out at the KREMS facility, which produced data suitable for use in initial evaluations of the proposed algorithm. Experiment #1 involved a satellite track made by ALCOR, while experiment #2 entailed the tracking of a calibration sphere by both ALCOR and MMW, for the HARP (High-Altitude Reconnaissance Platform) program. The details of these experiments, and analysis of their data, are described in the following sections.

4.1. Experimental Data

Experiment #1 was run on August 3rd. 1989, when a spherical satellite (LCS-4) was tracked from rising (at about 21° azimuth) to setting (at about 334° azimuth), by the ALCOR system at KREMS. At setting, the RCS of the satellite was observed to drop by approximately 3 dB due to weather of up to 35 dBZ in the area. Several PPI and RHI scans were taken by ALCOR along the satellite's trajectory, including an RHI scan at 333° azimuth and out to a range past the weather of interest, as shown in Figure 4.1. However, due to other commitments of the radar, no digitally recorded scans of the weather were made.

Experiment #2 was run on October 18th. 1988, when a 12 inch calibration sphere was dropped from an aircraft, and tracked by both ALCOR and MMW. The attenuation of the ALCOR signal was insignificant, but it was considerable for MMW, because the higher frequencies are more strongly attenuated. As a result, the data could be used to test only the algorithm for MMW. The sphere was initially picked up by the MMW radar at an elevation of 18.9° and an altitude of 12.6 km, and tracked as it fell, up to an elevation of 0.1°. It was initially 37.7 km from the radar, and its range decreased by only 1 km for the entire run. The azimuth was approximately 17° for the duration of the track.

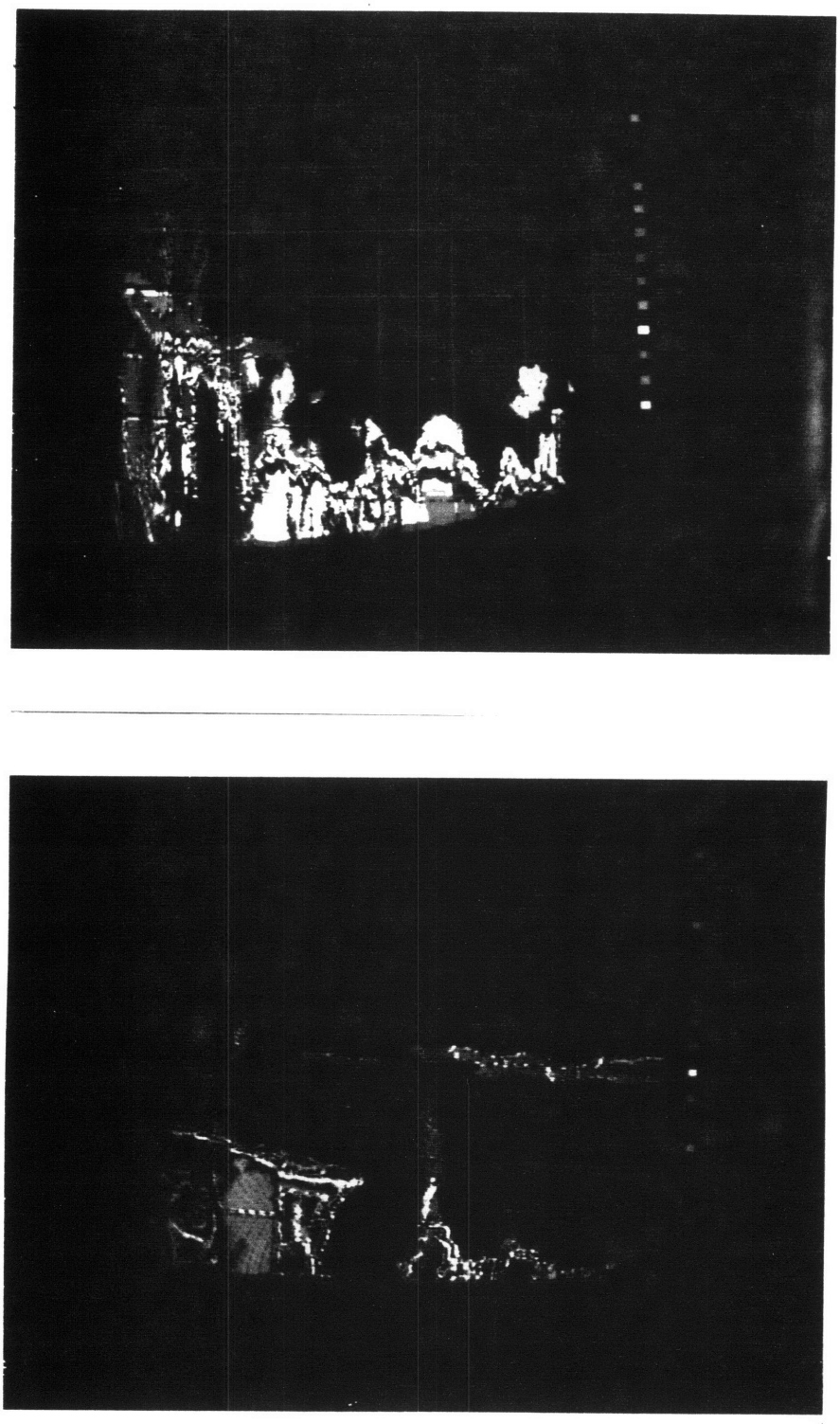

Figure 4.1 RHI scans for experiment #1 (top), used for the ALCOR algorithm, and experiment #2 (bottom), used for the MMW algorithm.

The attenuation of the MMW signal was initially about 3 dB, increasing to roughly 8 dB for elevations below 15°, and then 15 dB for elevations below 2.4° as the sphere fell behind increasing regions of precipitation. A RHI scan of the weather (shown in Figure 4.1), was taken by ALCOR 11 minutes prior to the sphere drop, at an azimuth of 15°, and out to a range of over 56 km, and showed precipitation levels in excess of 40 dBZ. Unfortunately, no digital recordings were available for this experiment.

4.2. Analysis of Data

The RHI scans of the weather (in Figure 4.1) were recorded by ALCOR for experiments #1 and #2, and used to test the performance of the proposed algorithm for ALCOR and MMW respectively. For experiment #1, the attenuation along the 0.6° elevation path was calculated from the relevant effective reflectivity factor values shown on the RHI scan, and then compared to the 3 dB value observed at setting (since this was the only occurrence of significant weather attenuation during the run). For experiment #2 however, the attenuation values along several different elevation paths were calculated. This was done for elevation angles of 1.8°, 2.4°, 5°, 7°, 10°, 11°, 12°, 13°, 15°, 16°, 17°, and 18.5°, and the results were plotted, together with the observed values, as a function of elevation angle.

In the analysis of the RHI scans shown in Figure 4.1, earth curvature effects were neglected for experiment #2, and the constant elevation paths were approximated by straight lines. For experiment #1 however, altitude values for the 0.6° elevation path were calculated every 32 km (see Appendix E) out to the full 224 km range of the RHI scan, and the path was approximated by a series of straight lines between these altitude points.

The depth of each range cell was measured, and then tabulated alongside the corresponding value for the effective reflectivity factor (hereafter referred to as the

reflectivity). The various reflectivity levels were indicated by different colours on the RHI scans, with contrasting colours representing adjacent levels (see Figure 4.1). These colours, and their values, were portrayed to the right of each scan, beginning at a 55 dBZ level, and increasing by 5 dBZ increments to 125 dBZ. The levels were marked by only the last two digits, so that values of 100 dBZ and above were wrapped around below the 55 dBZ mark.

For experiment #1, the displayed reflectivity levels were biased by 79.1 dBZ, so that this value had to be subtracted from the levels portrayed on the scan, in order to determine their actual values. These values were themselves corrected for attenuation due to the preceding range cells along the signal path, as explained in section 5.3.1. This was done only for experiment #1, since both the reflectivity levels and the RCS measurements were made by ALCOR, so that the attenuation of both sets of measurements were comparable.

For experiment #2, the attenuation of the reflectivity levels measured by ALCOR was a small fraction of the attenuation of the RCS measurements made by MMW. As a result, the indicated reflectivity levels were used directly, after being corrected for their 78.3 dBZ bias. For this experiment, a "bright-band" (as described in section 5.3.2) was identified in the RHI scan, so that only those reflectivity values lying below the altitude of the bright-band were used in the algorithm.

4.3. Measurement Accuracy

There were several aspects of the weather data measurement process, which impacted on the accuracy of the attenuation calculations, for both experiment #1 and #2. The RHI scans used for these experiments were not made along the exact azimuth of interest, falling short by 1° for experiment #1, and by 2° for experiment #2. The impact of

these deviations is minor for short ranges, but is quite significant at longer distances. For instance, a 1° shift in azimuth at 60 km corresponds to a deviation of over 1 km.

The RHI scans also were not made immediately following the RCS measurements. For experiment #2 there was an 11 minute time lag between the scan and the start of the target track, while for experiment #1 the scan was made approximately 30 minutes after the target track. The effects of these time lags will be examined later in section 5.2.

Another source of error in the calculations, is the fact that the reflectivity levels were measured by hand from the RHI scans. This required estimates of the depths of the range cells to a fraction of a millimeter, and for range cells of very high levels of reflectivity, a difference of as little as 0.2 mm would significantly affect the value of the total attenuation. Also, the straight-line estimates of the constant elevation signal paths would have caused some error in determining the reflectivity levels and the depths of the individual range cells. In addition, it was often difficult to differentiate between shades of the same colour in the RHI scans, and the wrong identification could result in a discrepancy of as much as 25 dB in the reflectivity value.

With the exception of the time lag problem, these sources of error can be reduced or eliminated by the use of digitally recorded weather scans, instead of the RHI or PPI scans, and more accurately directed range scans. The time lag problem is not so easily solved, and will be addressed in section 5.2. Also, the reflectivity measurements of the range cells are themselves attenuated by the presence of hydrometeors in the preceding range cells, and should not be forgotten, although this is a second order effect. However, the need to include corrections to the reflectivity measurements in the implementation of the algorithm, depends upon the level of accuracy required for the calculated attenuation.

4.4. Results

The experimental data was used to test which of the two Z-R relations, and which of the two k-R relations was most suitable, as well as the overall performance of the algorithm. The results of these tests are presented in the sections below, followed by a discussion of the results of including temperature variation into account for ALCOR.

4.4.1. Z-R Comparison

Plots were made of the calculated attenuation values using the Waldteufel k-R relations and the two Z-R relations, as shown in Figure 4.2 below. For both ALCOR and MMW, the Blanchard Z-R relation produced consistently higher attenuation values than those calculated using the Wexler and Atlas relations. In fact, there was a 44% difference in attenuation values for ALCOR, and a difference of about 11% for MMW. In both cases, the Wexler and Atlas Z-R relations gave results which were slightly closer to the observed values, and will be used in the further analysis.

4.4.2. k-R Comparison

Attenuation values were calculated for the two k-R relations, using the Wexler and Atlas Z-R relations. The results differed by 22% for ALCOR, and by 22 to 26% for MMW, as shown below in Figure 4.3. The Waldteufel k-R relations gave attenuation values which were in excellent agreement with the observed values for MMW, and similar results were obtained for ALCOR. For MMW the results were often within 1 dB of the observed values, and within 0.5 dB of the observed value for ALCOR.

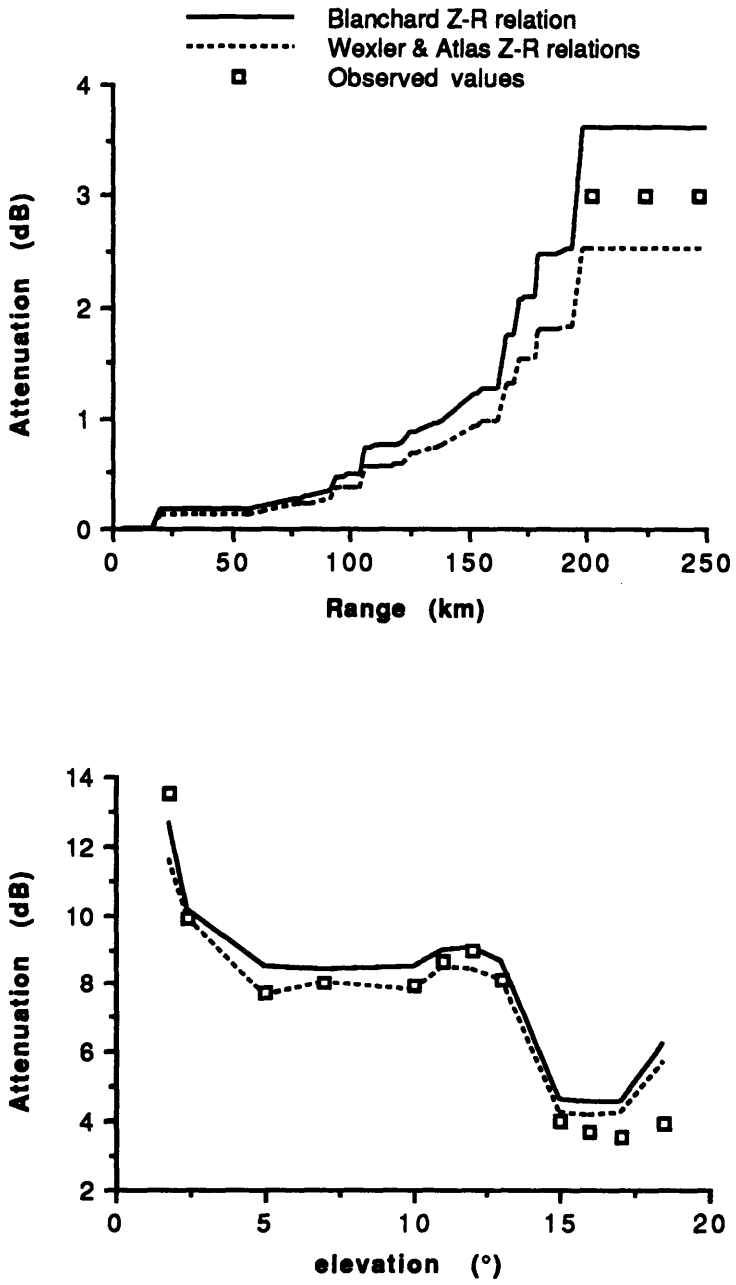

Figure 4.2 **Comparison of the Blanchard Z-R relation and the Wexler and Atlas Z-R relations, using the Waldteufel k-R relations and the data from experiment #1 for ALCOR (upper plot), and from experiment #2 for MMW (lower plot).**

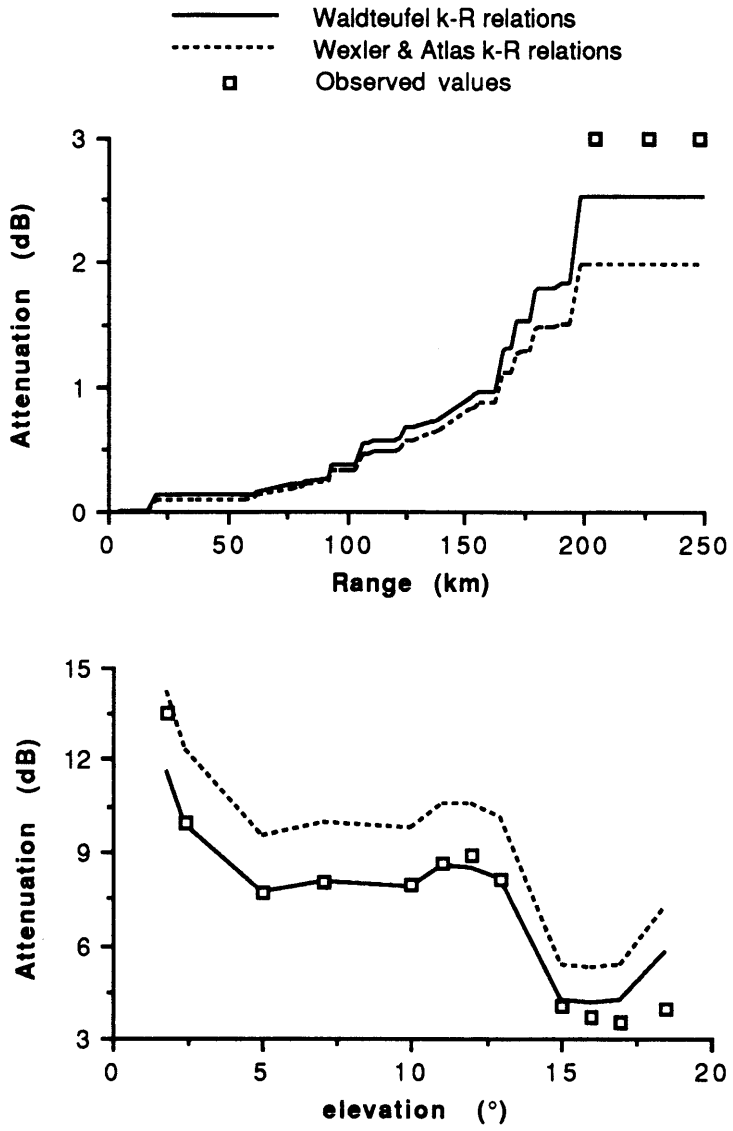

Figure 4.3 Comparison of the Waldteufel k-R relations and the Wexler and Atlas k-R relations, using the Wexler and Atlas Z-R relations and the data from experiment #1 for ALCOR (upper plot), and from experiment #2 for MMW (lower plot).

4.4.3. Temperature Variation Effects

In the prior runs, temperature effects were included in the analysis. In order to illustrate the importance of including temperature variation in the attenuation calculations, the results for ALCOR with a constant temperature assumption, and with the temperature

variation included, are shown in Figure 4.4. There was a significant difference in the total two-way attenuation values calculated using the two methods. In fact, the final attenuation level calculated using the variable temperature relationships was 23% greater than that for the constant temperature expression, and it was also closer to the observed value of 3 dB.

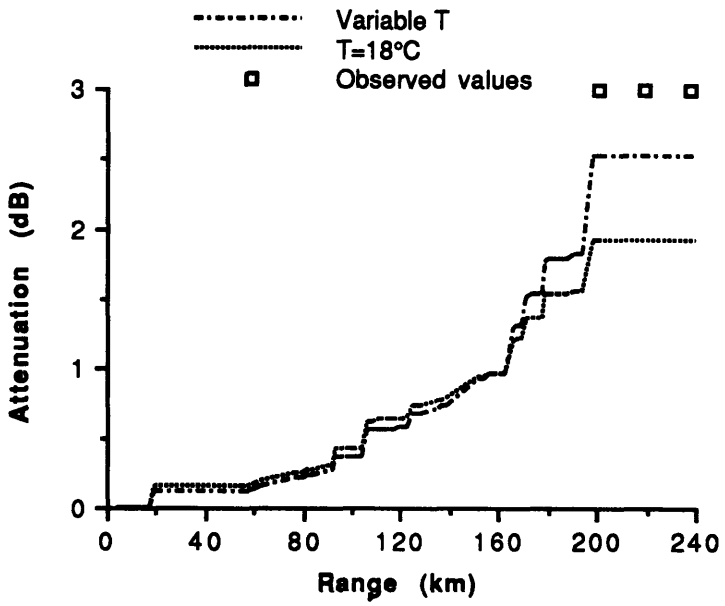

Figure 4.4 Effects of temperature variation on attenuation values for ALCOR (for data from experiment #1), using the Wexler and Atlas Z-R relations, and the Waldteufel k-R relations.

4.5. Conclusions

The results of applying the algorithm to these two data sets, indicate that it works well for MMW, as well as for ALCOR when temperature variation is included. The more analytic Wexler and Atlas Z-R relations gave slightly better results than the purely empirical Blanchard Z-R relation, while the Waldteufel k-R relations produced significantly better results than the Wexler and Atlas k-R relations.

However, due to the various sources of error in the measurement of the reflectivity levels, and the limited data available for validation, as well as in the assumptions made in the formulation the algorithm itself, these differences are not decisive. Therefore, either of the two Z-R relations, and either of the two k-R relations, could be used to produce adequate measures of the attenuation due to clouds or rainfall. Nevertheless, it is the opinion of the author that the Wexler and Atlas Z-R relations, combined with the Waldteufel k-R relations, would be best for use in the algorithm, and the steps of this recommended algorithm are outlined in Figure 4.5 below.

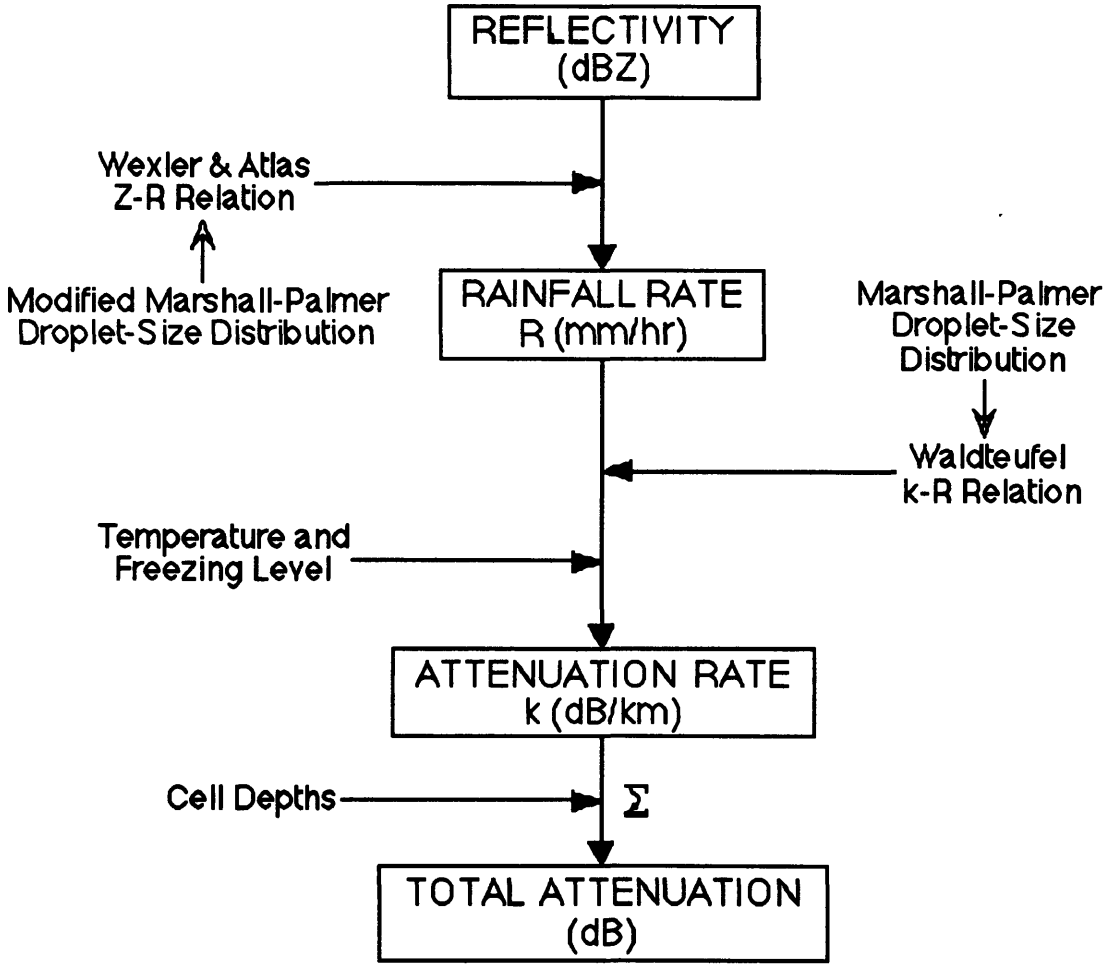

Figure 4.5 Structure of the recommended attenuation algorithm

5. Implementation Issues

The implementation of an algorithm such as this is difficult, due to the problem of obtaining timely weather scan data to calculate the attenuation. Ideally, the weather scans should be made along the identical signal paths, while the target is being tracked. However, this is not usually feasible for a single radar, and even if a different radar were to be used for the range scans, it would not be able to make many scans while the target was being tracked, because of the high speed at which the target would be falling, and the resulting high slew rate of the antenna.

Implementation issues are addressed in the following sections, beginning with desirable scanning procedures. This is followed by a determination of the time scales during which meaningful measurements may be made, and an examination of application issues. Finally, the possibility of applying the algorithm to the problem of establishing meaningful criteria for mission aborts is investigated.

5.1. Scanning Procedures

For maximum accuracy, the range scans of the weather should be recorded in digital form, as is done for the MOIST programs mentioned in Chapter 2. RHI scans may be used, but these require that the reflectivity values and signal paths be evaluated by hand, which diminishes accuracy significantly.

Range scans along the target azimuth and elevation should be made immediately prior to, or immediately after, a target track. Taking the range scan after the track would be preferable, since the target's exact trajectory would then be known. Also, once the target track has been made, any region of sudden or large changes in the RCS value can be identified to ensure that such regions are not over-looked.

The range scans should be made in the direction of selected points along the target's trajectory, beginning at the lowest elevations where weather is most likely to be a problem, and moving upward. As many points as possible should be selected, with emphasis on regions of sudden or large changes in RCS values. The scans need not be made further out than the range of the target trajectory, unless there is a large time lag between the RCS measurements and the range scans, during which the weather cells have moved further away from the radar.

Weather cells do move (advect), as well as change in structure and intensity, over time, causing large errors in attenuation estimates if the recommended weather scans are made at some time considerably after the RCS measurements. The following section investigates the time scales over which cell movement, and changes in cell composition, are likely to affect the application of the algorithm. Methods are recommended for dealing with this problem.

5.2. Relevant Time Scales

In order to determine reasonable time frames during which range scans remain useful, periodic PPI scans of weather over Kwajalein were analyzed. These scans were made every five minutes at an elevation of 1.2°, and out to a range of 120 km, as part of the ground truth data collected for the NASA Tropical Rainfall Measurement Mission (TRMM). The scans for six days, spanning the months of January to April 1990, were obtained from NASA for analysis. These days were chosen for seasonal variety, as well as the occurrence of high amounts of rainfall. The presentation and analysis of the data are outlined in the sections below, followed by an overview of the measurement errors, and results of the analysis.

5.2.1. NASA TRMM Historical Reflectivity Data

The PPI scans obtained from NASA were recorded as computer text files, with the different reflectivity levels being represented by ASCII characters, so that they could be printed out for inspection. A printout of typical PPI scan is shown below in Figure 5.1.

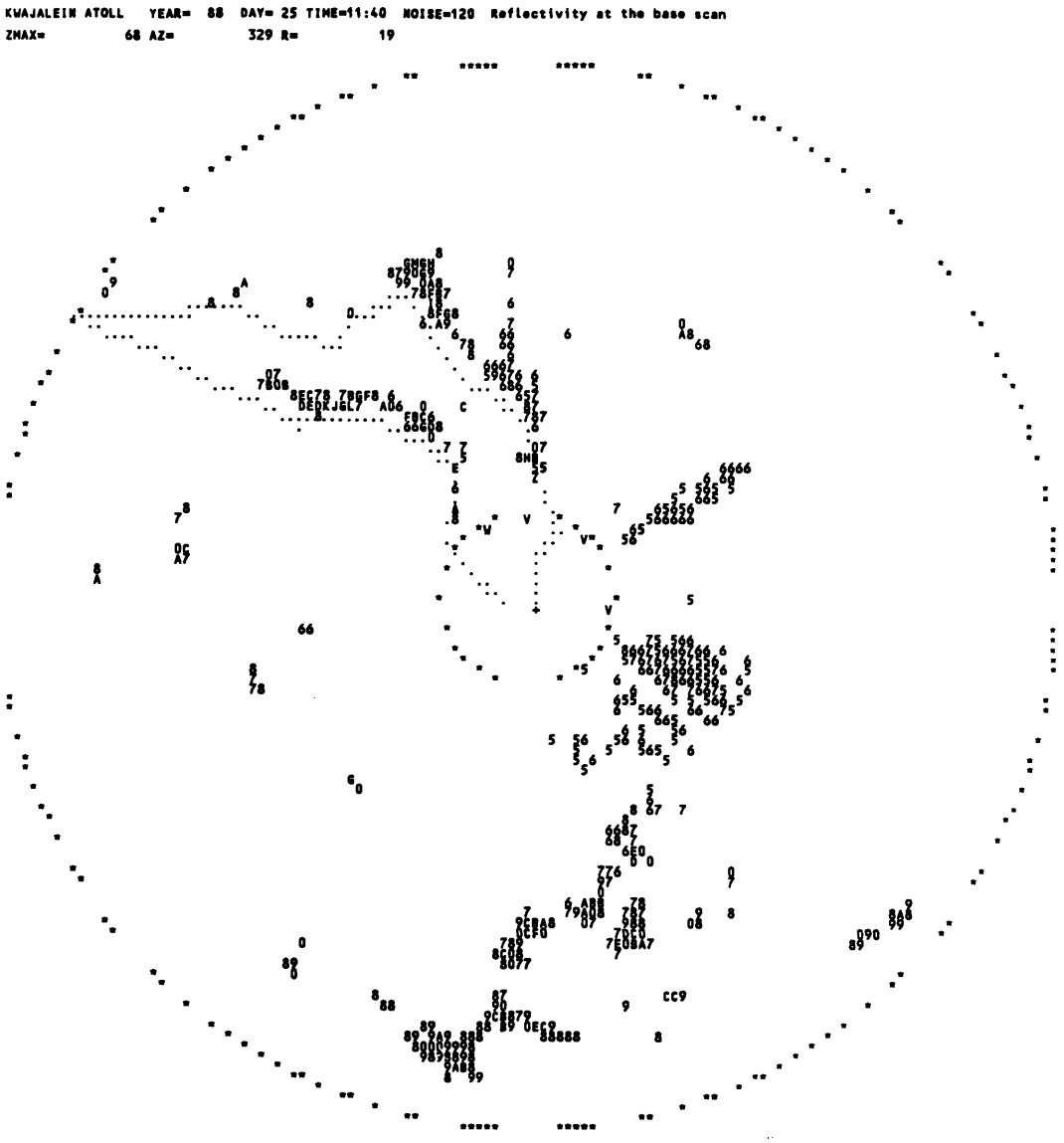

Figure 5.1 Presentation of a typical PPI scan from the NASA TRMM data.

The scans were made by a WSR-74 S-band weather radar located on Kwajalein island, which is situated on the southernmost tip of the Atoll. The radar is indicated on the PPI scans by the plus (+) character, as shown in Figure 5.1. The 20 km and 120 km range circles are marked by the asterisk (*) character, and the Kwajalein Atoll is outlined by dots. The date and time of each scan are also listed above the map, followed by an indication of the noise level, and the position and value of the maximum reflectivity level. However, the maximum reflectivity is often a result of sea-level clutter, such as ships, as in the case of the scan shown in Figure 5.1.

The radar reflectivity levels of the weather are represented consecutively by the numbers from 1 to 9, followed by 0, and then by the letters from A to Z. The reflectivity levels begin at 3 dBZ, and then increase in 2 dB steps for each successive character. The area covered by each character corresponds to a rectangle of approximately 0.9 km from east to west, and 1.2 km from north to south. The individual cells were rectangular instead of square, because of the typical height to width ratio of the characters used. This cartesian representation of the weather was derived from a transformation of the original polar coordinates, producing discretization errors in the reflectivity levels. This transformation also causes a loss in resolution for measurements made close in to the radar.

The PPI scans were difficult to use in this format. Variations in the reflectivity levels were not readily apparent, and it was virtually impossible to see changes from one scan to the next, because of the large number of levels displayed, as well as the need to translate the characters to their corresponding reflectivity levels. Therefore, the presentation of the PPI scans was modified, as shown in Figure 5.2, so as to facilitate analysis of the data. This was done by separating the reflectivity levels into eight groups, as listed in Table 5.1, with each successive group being represented by a darker shade of grey.

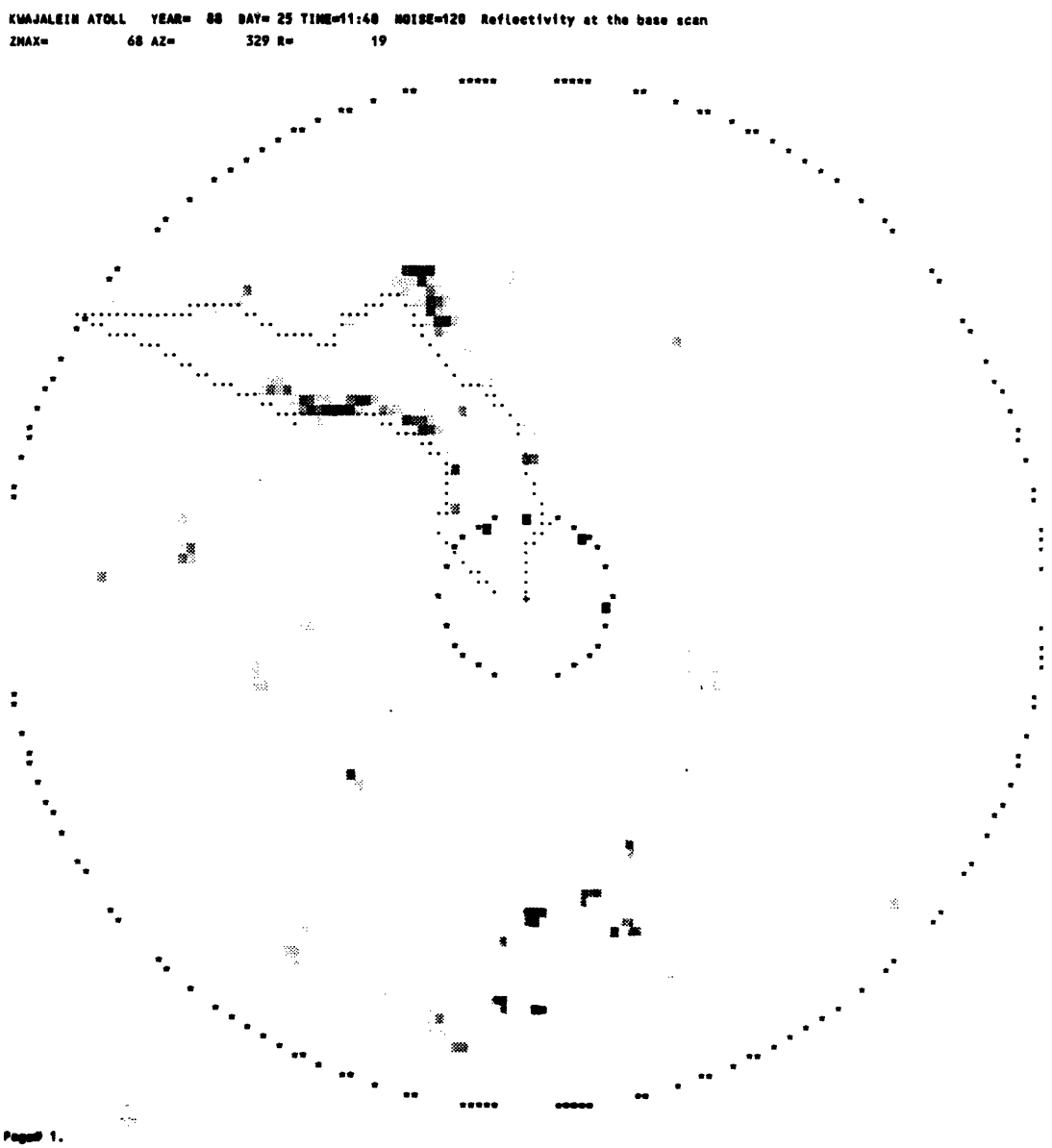

Figure 5.2 Presentation of modified PPI scan from the NASA TRMM data.

Group #	Reflectivity Range (dBZ)
1	≤ 14
2	15 to 22
3	23 to 30
4	31 to 38
5	39 to 46
6	47 to 54
7	55 to 62
8	≥ 63

Table 5.1 Grouping of reflectivity levels used to modify to PPI scans from the NASA TRMM data.

5.2.2. Time Scale Analysis of TRMM Data

The analysis of this TRMM data was undertaken in an attempt to determine the time scales over which there was significant change in weather attenuation. This was done by calculating the total attenuation, for both ALCOR and MMW, along signal paths of constant azimuth from the WSR-74 radar located on Kwajalein. The attenuation values were calculated at ten minute intervals over a period of two hours, and then plotted as a function of time. Since most reentry field tests at the KREMS facility are carried out toward the northeast of the Atoll, the 45° azimuth was used as the baseline for these calculations. However, the 135° and 315° azimuths were also used for comparison. Five periods were evaluated for the 45° azimuth and three of these for the 135° and the 315° azimuths.

The attenuation values were calculated by drawing a line from the radar to the outer range circle at the particular azimuth, and then summing the contributions to attenuation due to each 'box' of weather intersecting the line. The intersecting width of each cell was estimated as a fraction of the diagonal length of a cell, and the average of the reflectivity levels (in dBZ) in each grey-scale group was used in the attenuation calculations. The k-R relations used for the calculations were derived from the Waldteufel k-R relations, and the Wexler and Atlas Z-R relations, and were valid for reflectivity levels of up to 42 dBZ. These modified k-R relations were also used in the development of the abort criteria curves, shown in section 5.4 below, and are given in Appendix G.

The overall movement of the weather cells was also evaluated, by estimating the number of spaces to the east and to the north, which had been traversed by most of the weather cells, in the five minutes between scans. These distances were then used to determine the average speed of the weather cells, by dividing the distance travelled since the previous scan, by the intervening 5 minutes. The direction of the cell motion, at the time of each scan, was also determined from the displacement of the weather cells, from their positions in the preceding scan. These displacement estimates were made over a period of 75 minutes on four different days, and the results are presented in section 5.2.4, together with the attenuation values along the 45°, 135°, and 315° azimuth paths.

5.2.3. Measurement Errors

In order to properly evaluate these results, one must be aware of the level of accuracy in these measurements. Since the attenuation values were calculated from the average reflectivity level for each grey-scale group, they could have been anywhere from one half to two times the actual attenuation values. Also, the cell depths were estimated in quarters of the diagonal length of a 'box' (1.49 km), introducing a further error in the attenuation value, for each box which intersects the path for only a fraction of a diagonal.

There is also some level of uncertainty in the reflectivity values themselves, and these errors can accumulate, thereby producing a large amount of 'noise' in the attenuation results. This is not considered critical however, since only trends in attenuation variability were of interest.

There are similar sources of error in the evaluations of the weather cell movements. The distances travelled by the weather cells, to the east and north, were estimated in terms of 'box' lengths, generating a possible error of half a 'box' length in the displacement values (0.46 km east-west, and 0.585 km north-south). Also, these displacements were estimated by viewing the weather over the entire scan, and not any one cell in particular. As a result, the displacement uncertainty is even larger, but it is not possible to determine an exact value for this source of error. There was also some variation in the time between scans, by as much as one minute. These uncertainties can result in cell speed errors of approximately 10 km hr^{-1}, and errors in the direction of the cell motion of up to 90° of azimuth in extreme cases.

5.2.4. Results

The plots of the attenuation values calculated for MMW parameters along the 45° azimuth path are shown in Figure 5.3, followed by Figure 5.4, which displays the corresponding plots for the 135° and 315° azimuth paths. The plots of the attenuation values for ALCOR, which are shown in Appendix F, follow the same trends, but with smaller levels of attenuation. These attenuation values are quite erratic during periods of precipitation, but occasionally exhibited short periods of steadiness. However, it is evident from inspections of the weather scans themselves, that these variations in the attenuation values are due largely to the advection of weather cells across the azimuth paths. This can be seen in the sample scans shown in Figures 5.5a through 5.5c, which correspond to the data for day 41, 1990 (February 10th. 1990).

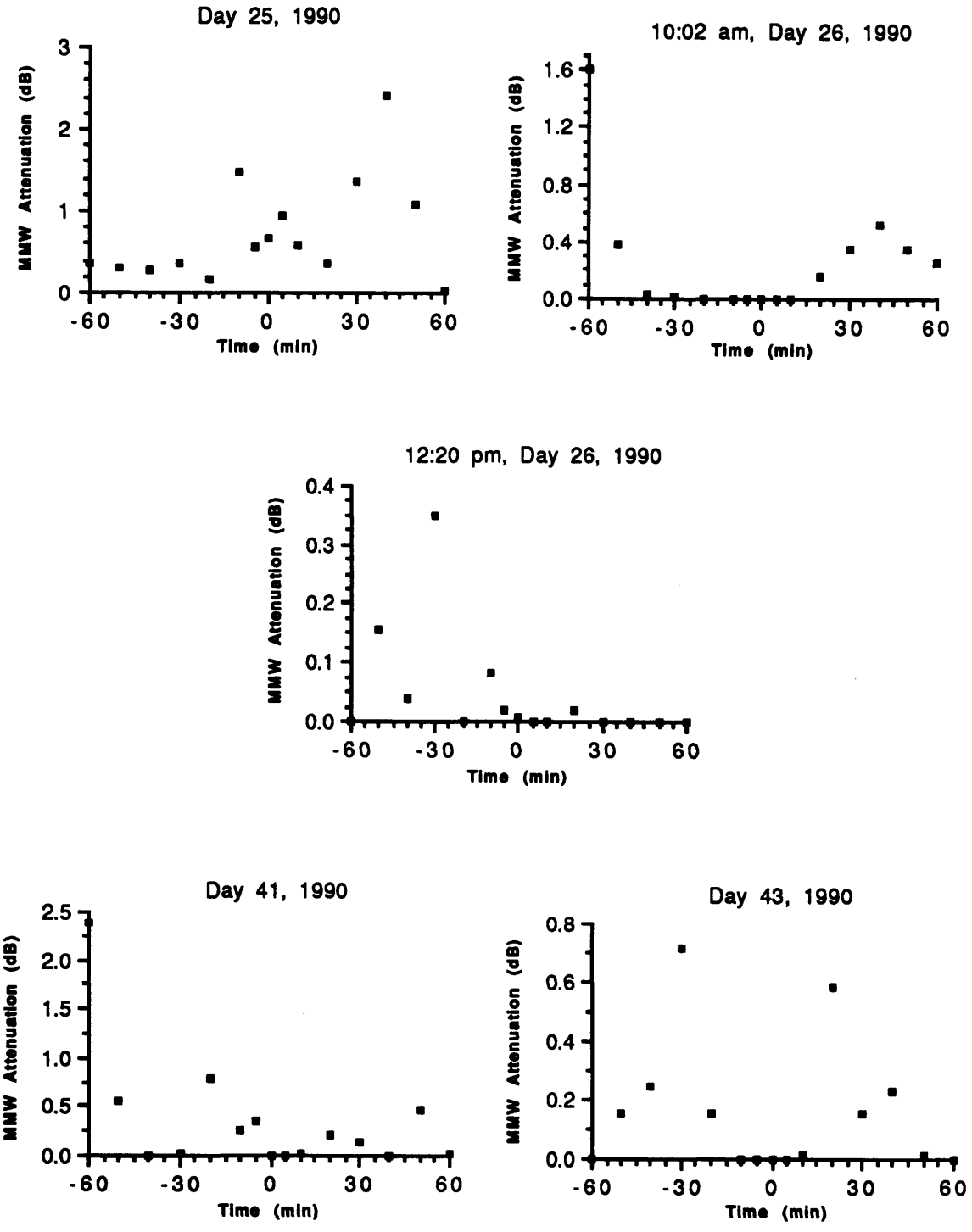

Figure 5.3 Plots of calculated attenuation along the 45° azimuth on four different days, from the NASA TRMM data.

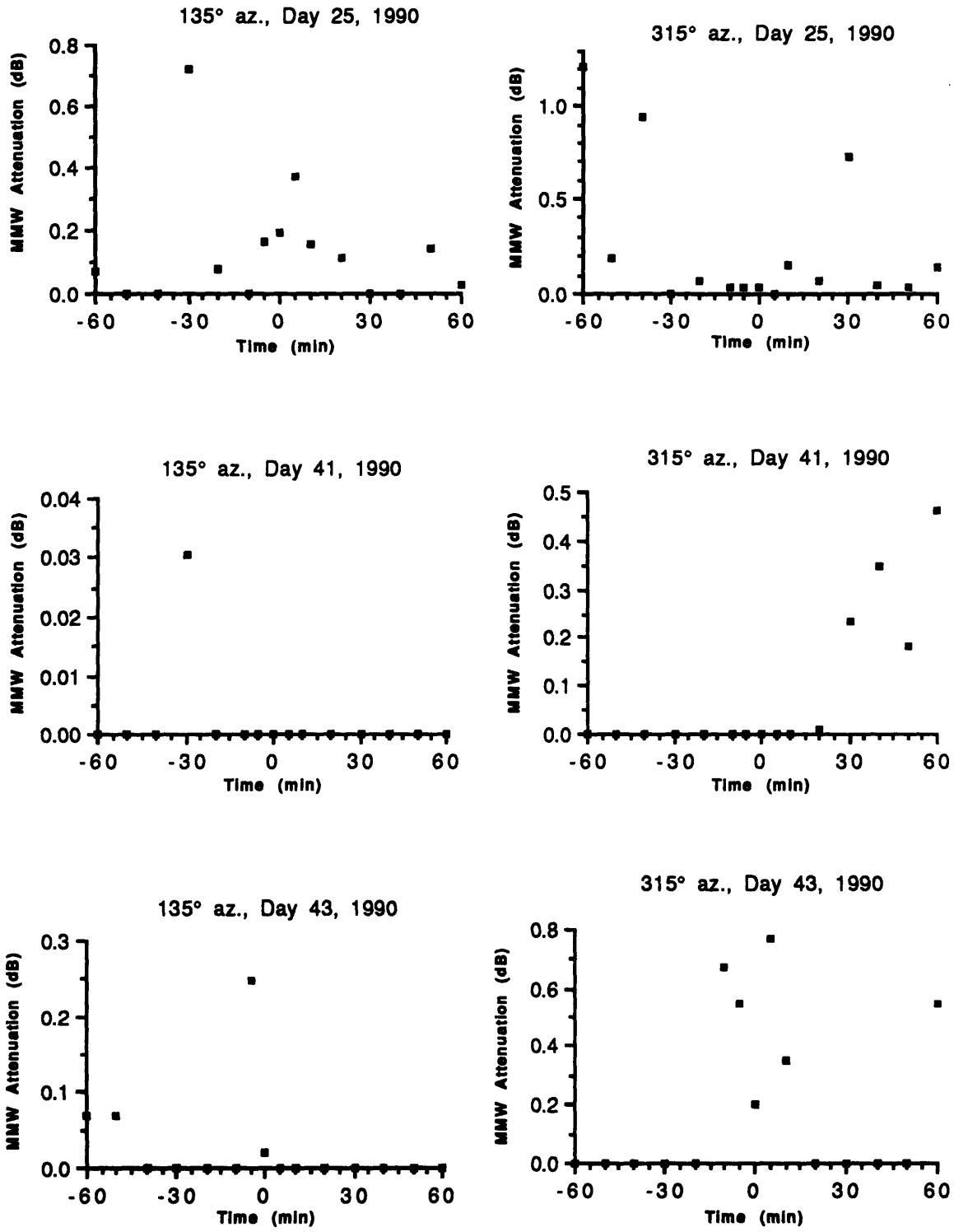

Figure 5.4 Plots of calculated attenuation along the 135° and 315° azimuths on three different days, from the NASA TRMM data.

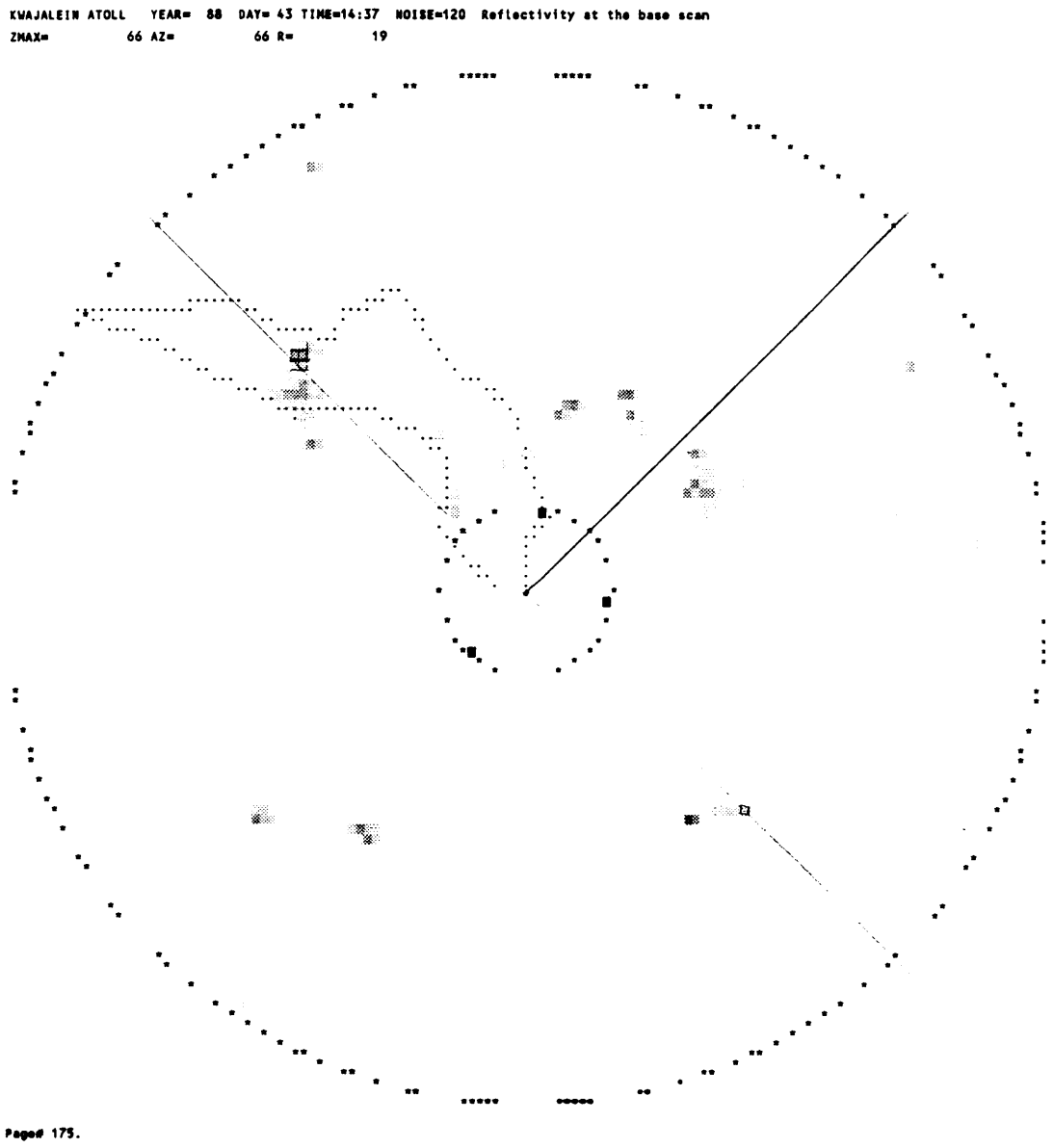

Figure 5.5a Demonstration of cell movement in three consecutive PPI scans from the NASA TRMM data.

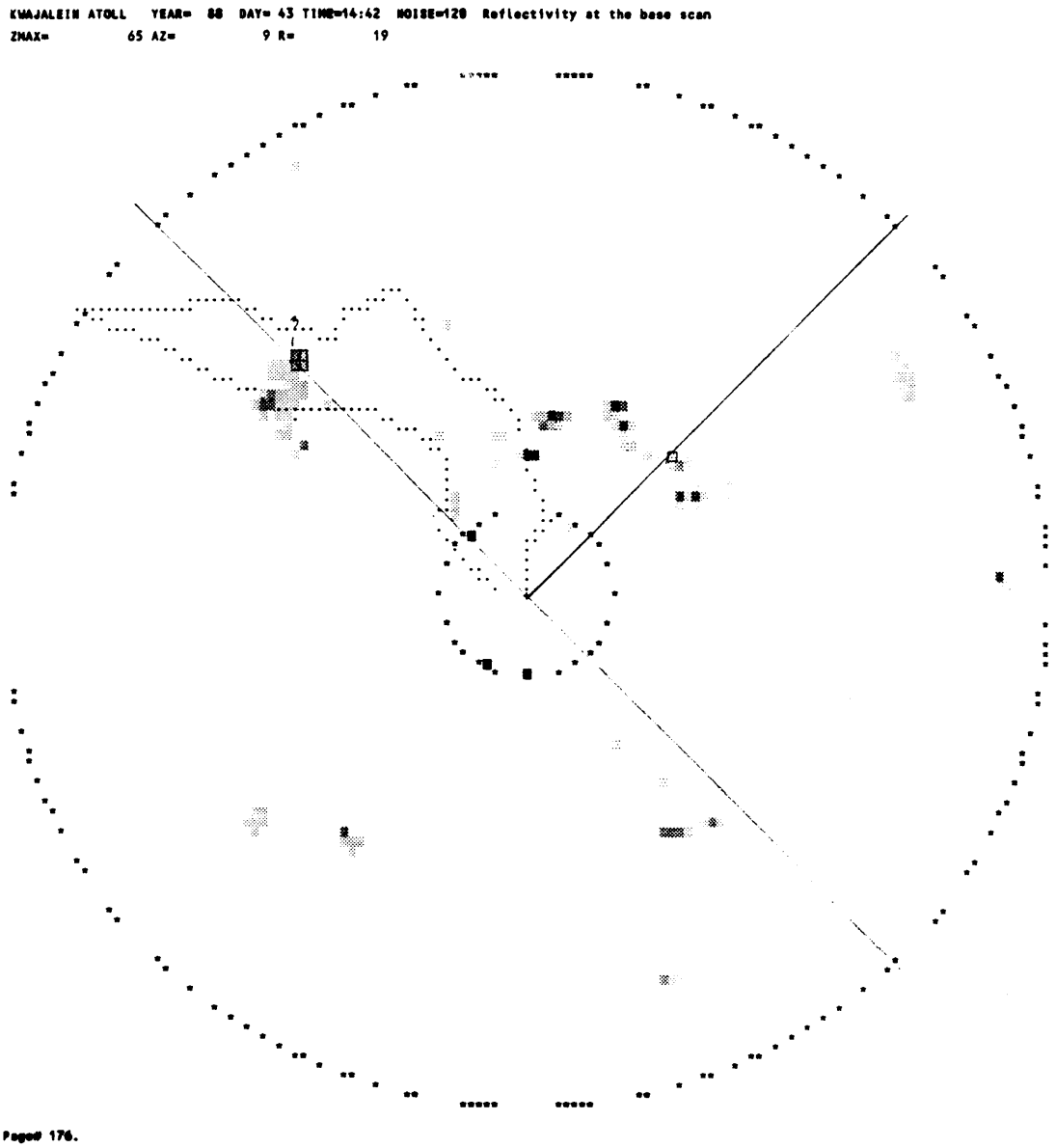

Figure 5.5b Demonstration of cell movement in three consecutive PPI scans from the NASA TRMM data (cont'd).

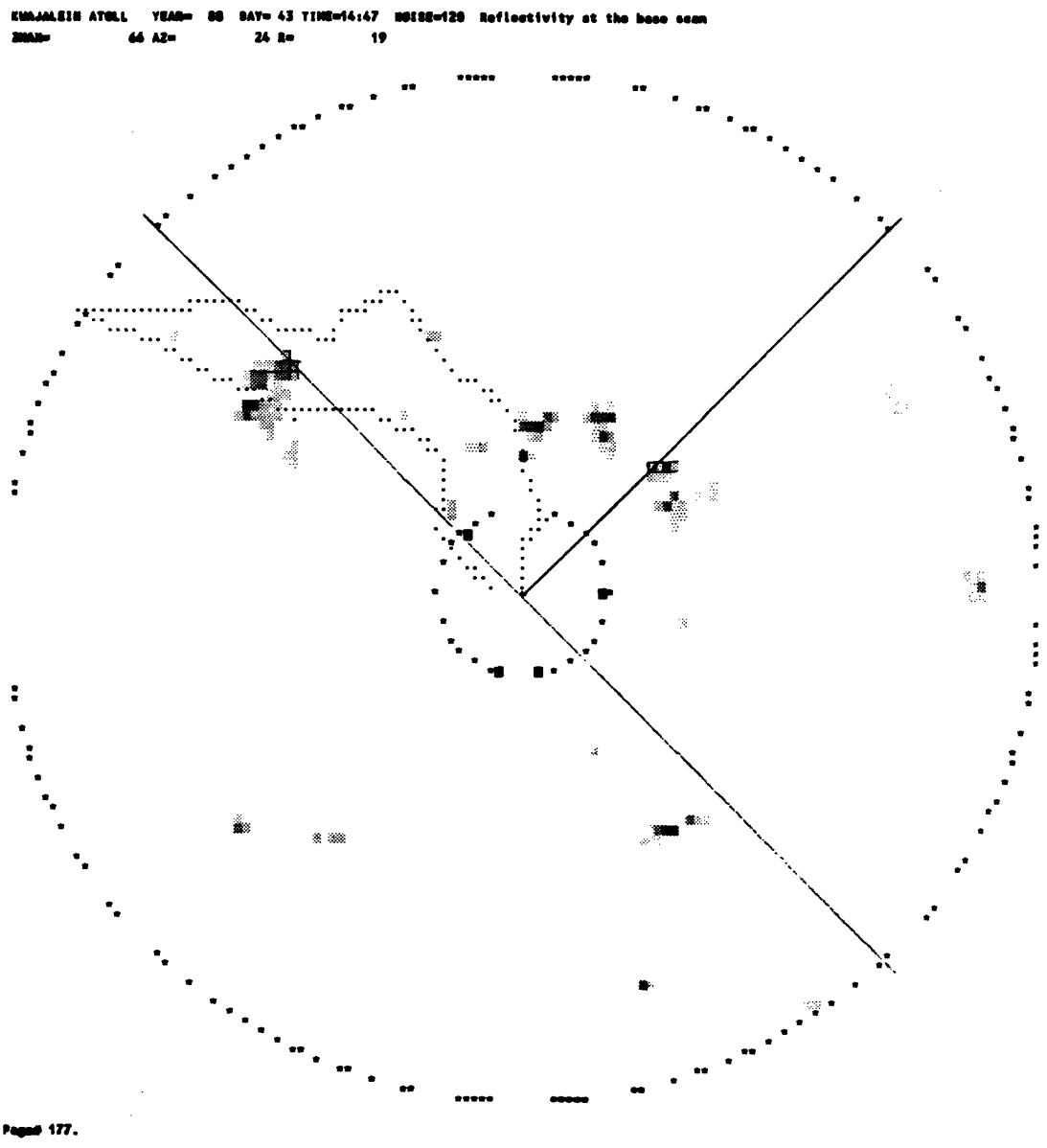

Figure 5.5c Demonstration of cell movement in three consecutive PPI scans from the NASA TRMM data (cont'd).

The characteristics of the weather cell advection can be examined from the plots of weather cell speed, and direction of motion, which are shown in Figures 5.6 and 5.7. There is a 20 minute period of erratic variations in cell speed on day 26, as well as on day 91, and similar variations throughout for day 41, but these variations are largely on the order of the predicted 10 km hr^{-1} of measurement noise. The results for day 25 do display significant changes in cell speed, which appears to be generally increasing in the latter half of the hour. However, the overall trend appears to be a relatively steady level of cell speed over these time periods.

As shown in Figure 5.7, the direction of cell motion was also relatively constant, not only for each day, but also from one day to the next. The cell direction was generally toward the east, but with a northward component on day 41, a southward component on day 26, and a change toward the south during the latter half hour, on day 25.

These attenuation and cell advection measurements indicate that weather scans, which are made even as much as ten minutes before or after the RCS measurements, are not likely to be useful if applied directly. Therefore, the proposed attenuation algorithm can only be directly applied if weather scans are made immediately following the RCS measurements.

However, if such immediate range scans are not feasible, it may be possible to predict the occurrences of weather attenuation along any given azimuth, due to the relative consistency in cell advection. Cell advection is due primarily to the winds in the region. Therefore, prior weather scans could be made upwind of the target trajectory, to determine the likelihood of weather cells moving into the path of the radar signal during the target track. These weather scans can be made before the target track, and used to evaluate the speed of any weather cells moving toward the test area. If there are weather cells moving

toward the test area, their speeds can be used to estimate the times at which they will arrive, and these times can then be avoided.

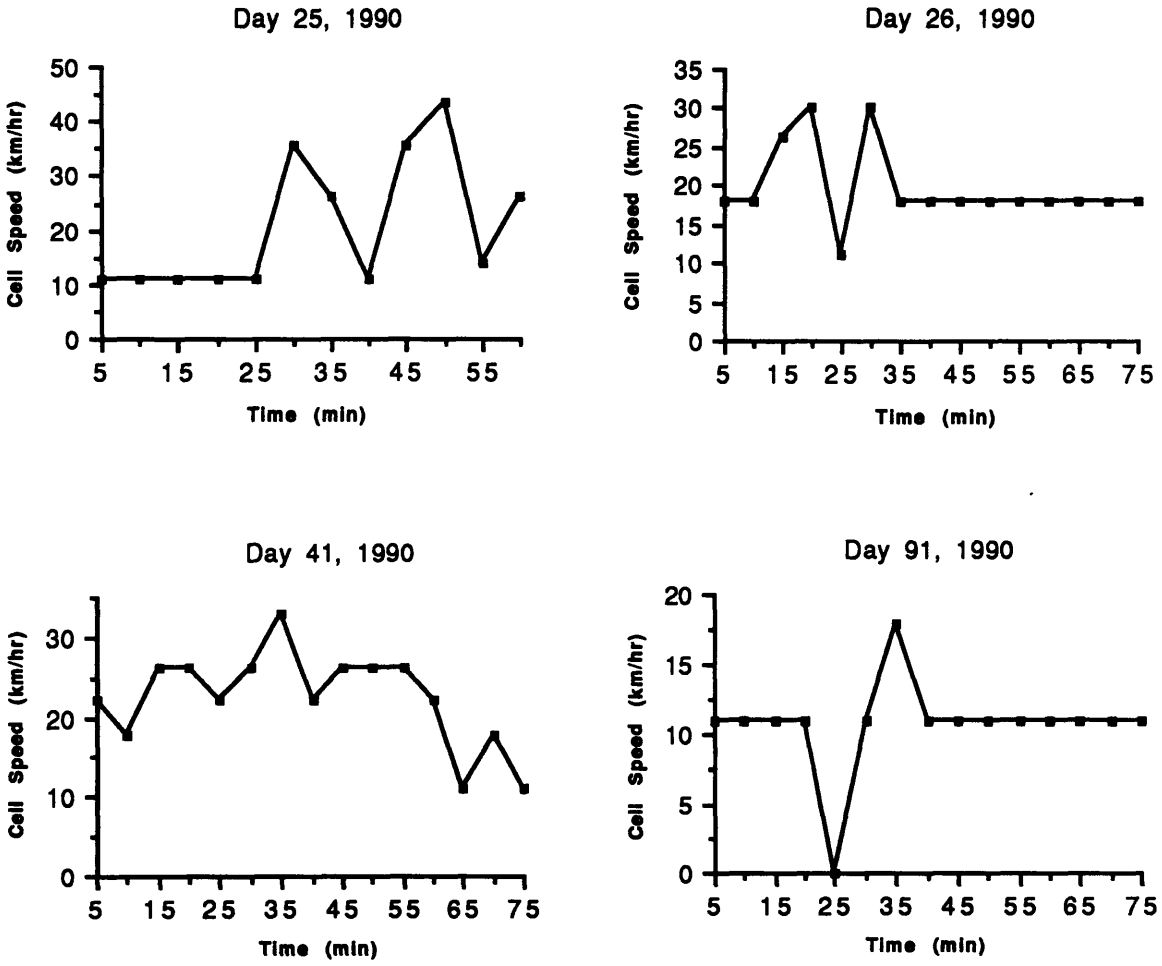

Figure 5.6 Plots of overall cell speed calculated on four different days, from the NASA TRMM data.

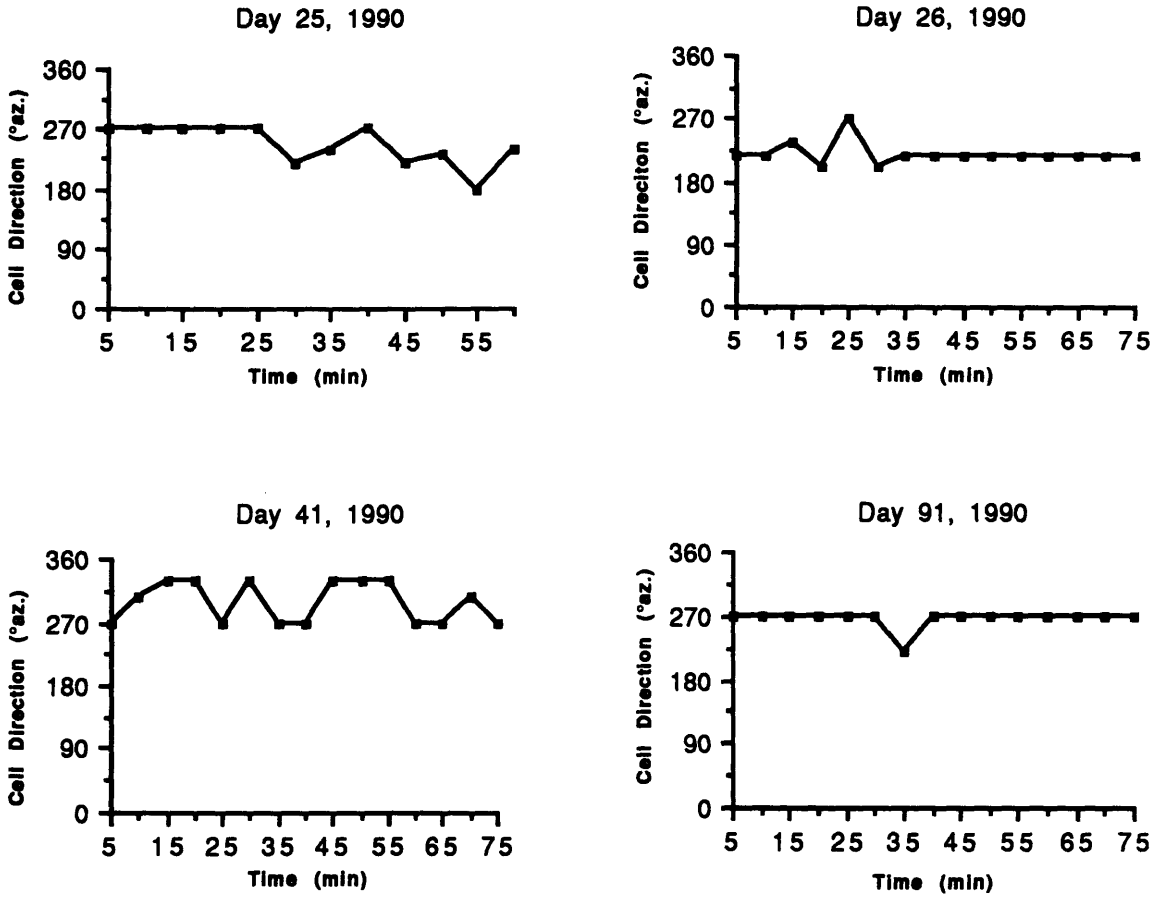

Figure 5.7 Plots of direction of cell movement calculated on four different days, from the NASA TRMM data.

If it is impossible to avoid occurrences of weather attenuation, and a time lag between the RCS measurements and the weather scans cannot be prevented, the algorithm may still be used. If the weather cell advection is also known, then the range scans of the weather can be made along azimuths which are corrected to account for the movement of the weather cells. This procedure is valid only if the time between the weather scans, and RCS measurements, is not long enough for significant changes in cell structure to occur.

5.3. Identification of the Freezing Level

Once timely measurements of the reflectivity levels of the weather have been made, the problem of actually applying the algorithm may be tackled. It was demonstrated earlier (in Chapter 3) that the attenuation due to ice clouds is considerably less than that due to water clouds, and may therefore be neglected from the weather attenuation calculations. Nonetheless, an identification of the level at which freezing occurs in clouds is still necessary.

Of even greater importance is the identification of the "bright-band" which is sometimes present in cloud cells. The bright-band is a layer of melting snowflakes, which generate extremely high Z_e levels because of their non-spherical shapes and dual-phase composition. Despite these large Z_e levels, their attenuation cross-sections are generally comparable to those for water spheres of equal volume, so that use of these high Z_e levels in the algorithm would cause a great over-estimation of the weather attenuation. As a result, only those Z_e levels occurring below the bright-band should be considered in the proposed algorithm, and this is currently possible only if the weather scan is checked by hand. This was done for both experiment #1 and #2, but no bright-band was encountered along the 0.6° elevation for experiment #1.

However, the necessity for human intervention does significantly increase the time required to run the algorithm, and an automatic identification of the freezing level would be better. The MOIST programs, which were described in Chapter 2, make the assumption of a constant altitude freezing level at 4.6 km, and this would be the simplest criterion for the algorithm if it were to be used in tandem with the MOIST programs. However, when the freezing level was set at the altitude of 4.6 km in the calculations for experiment #2, there was a 142% change at the 16° elevation, where the bright-band extended down to an altitude of 4.4 km.

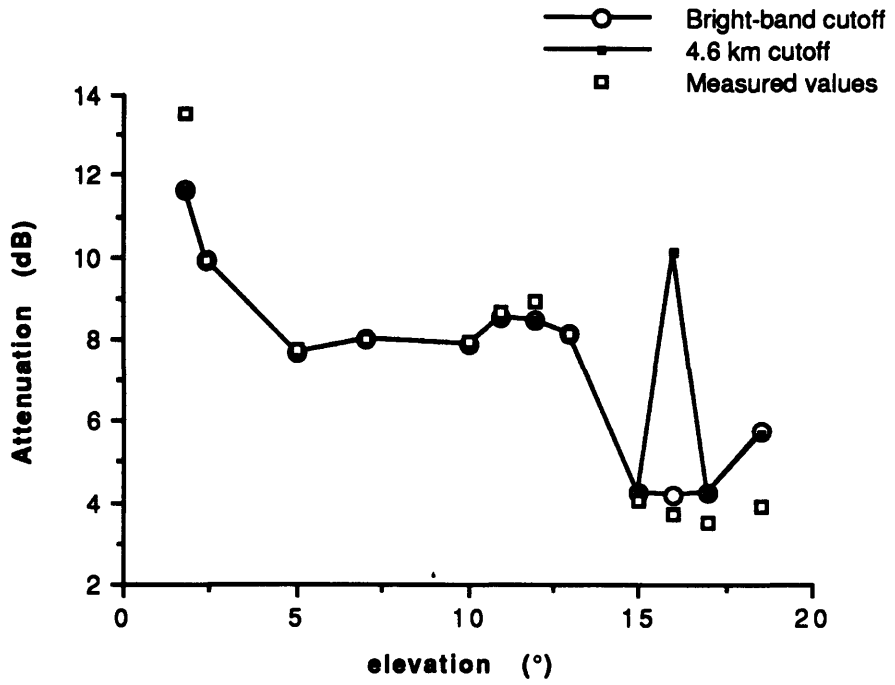

Figure 5.8 Attenuation values calculated for MMW from the data in experiment #2, using the 4.6 km altitude cutoff, and identification of the bright-band.

Another possibility would be to use a cutoff altitude at a fixed distance below the 0°C isotherm so as to exclude the bright-band (Battan (1973) states a bright-band depth of 500 meters). The altitude of the 0°C isotherm could be found from daily temperature soundings, or from the annual reference atmosphere for Kwajalein which is already used in the algorithm to determine the temperature of the range cells. Of course, if there are daily temperature soundings available, these would be preferable for use in the algorithm rather than the annual reference atmosphere listing. This method is recommended for avoiding bright-band effects, particularly if daily temperature soundings are available.

5.4. Abort Criteria

At present, missions at KREMS which utilize the MMW radar are aborted if weather scans show a peak reflectivity of 35 dBZ or more in the area. This criterion can be quite misleading, since the item of concern is actually the total attenuation, and not the peak reflectivity of the weather. It is possible for a weather cell with a peak reflectivity of only 25 dBZ to cause greater attenuation than a smaller cell whose peak reflectivity is 45 dBZ. Using the proposed attenuation algorithm, and two simple weather cell models, curves of peak reflectivity versus cell diameter, for different values of total attenuation, were produced for use in establishing mission abort criteria based on PPI scans.

One of the models (model #1) used for the weather cell assumed a constant level of reflectivity throughout. The other model (model #2) assumed a Gaussian distribution of reflectivity levels across its diameter, dropping by 20 dB at the edge from its peak value in the center, but without the required integrated value of unity. This distribution was chosen because it represents the tendency of cloud cells to be most intense at the center, particularly during periods of strong convection, and then tapering off toward the edges. For both models, the weather cell was assumed to be cylindrical, with infinite height and a vertically uniform reflectivity level distribution, so that the elevation of the scan was inconsequential.

For model #2, the reflectivity at a distance x (in km) from the center of the cell could be expressed by the Gaussian-like function

$$Z = Z_0 e^{-\pi(x Z_0 / C)^2} \tag{5.1}$$

for Z in $mm^6 m^{-3}$, where Z_0 is the peak reflectivity, and C is a constant which scales the integral to any value, not necessarily unity. The structure of this function can be seen in Figure 5.9, where Z is plotted as a function of x, for Z_0 = 30 dBZ and C = 50 dB. The structure for weather cell model #1 is also shown in Figure 5.9.

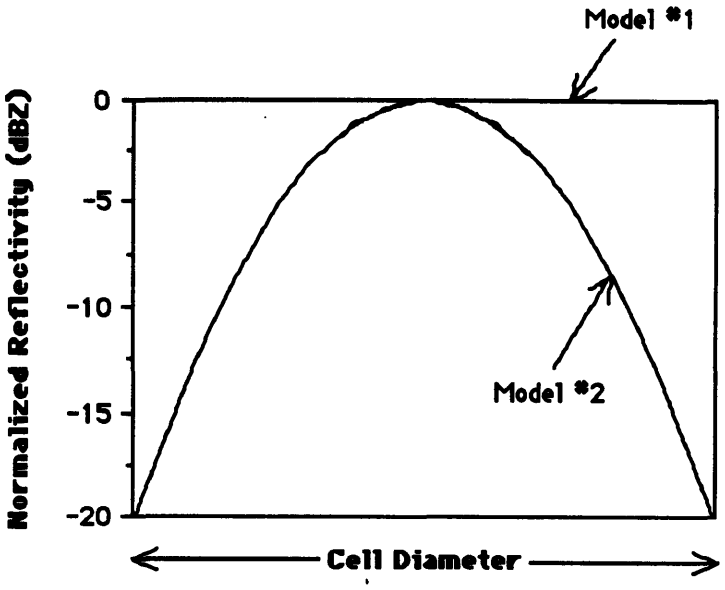

Figure 5.9 Distribution of reflectivity levels in the two weather cell models.

The total two-way attenuation, A_2 in dB, for the two radars could then be calculated by substituting appropriate k-Z relations into equation (5.1), and integrating across the diameter of the weather cell (see Appendix F for details). The resulting expressions, for ALCOR and MMW respectively, were

$$A_{2A} = 2.64\text{x}10^{-5}\, d\, Z_o^{0.8} \tag{5.2}$$

and

$$A_{2M} = 1.28\text{x}10^{-3}\, d\, Z_o^{0.83} \tag{5.3}$$

where d = cell diameter in km.

By re-arranging equations (5.2) and (5.3), the peak reflectivity of the weather cell could be expressed as a function of cell diameter, and total two-way attenuation, with

$$Z_o = 5.28\text{x}10^5 \left(\frac{A_{2A}}{d}\right)^{1.25} \tag{5.4}$$

for ALCOR, and for MMW

$$Z_o = 3.0 \times 10^3 \left(\frac{A_{2M}}{d}\right)^{1.2} \qquad (5.5)$$

Attenuation values of varying intensity are of concern for different missions at the KREMS facility. Therefore, curves of Z_o versus d were plotted for attenuation values of 1, 3, 10, 15, and 20 dB for MMW, which are typical at such wavelengths, while values of 0.1, 0.5, 1.0, 3.0, and 5.0 dB were used for ALCOR (see Figure 5.10). A similar set of curves were also plotted for the constant reflectivity structure of weather cell model #1, and these are shown in Figure 5.11.

These curves may be used in the following manner, to determine whether a mission should be aborted due to the presence of weather in the area. For any given field test, there is some maximum amount of weather attenuation which can be tolerated, or else the test must be aborted. The diameter, and the peak reflectivity level, of any weather cell which may advect into the test area, can be estimated from a PPI scan, and the corresponding point plotted on the graphs of Figure 5.10 or 5.11. It will then be immediately apparent whether or not that point lies above or below the curve for the permissible amount of attenuation. If it is below the curve, then the attenuation due to the weather cell would be under the critical level, and the test may proceed. Of course, if there are a number of weather cells present, then the attenuation due to each cell would be cumulative.

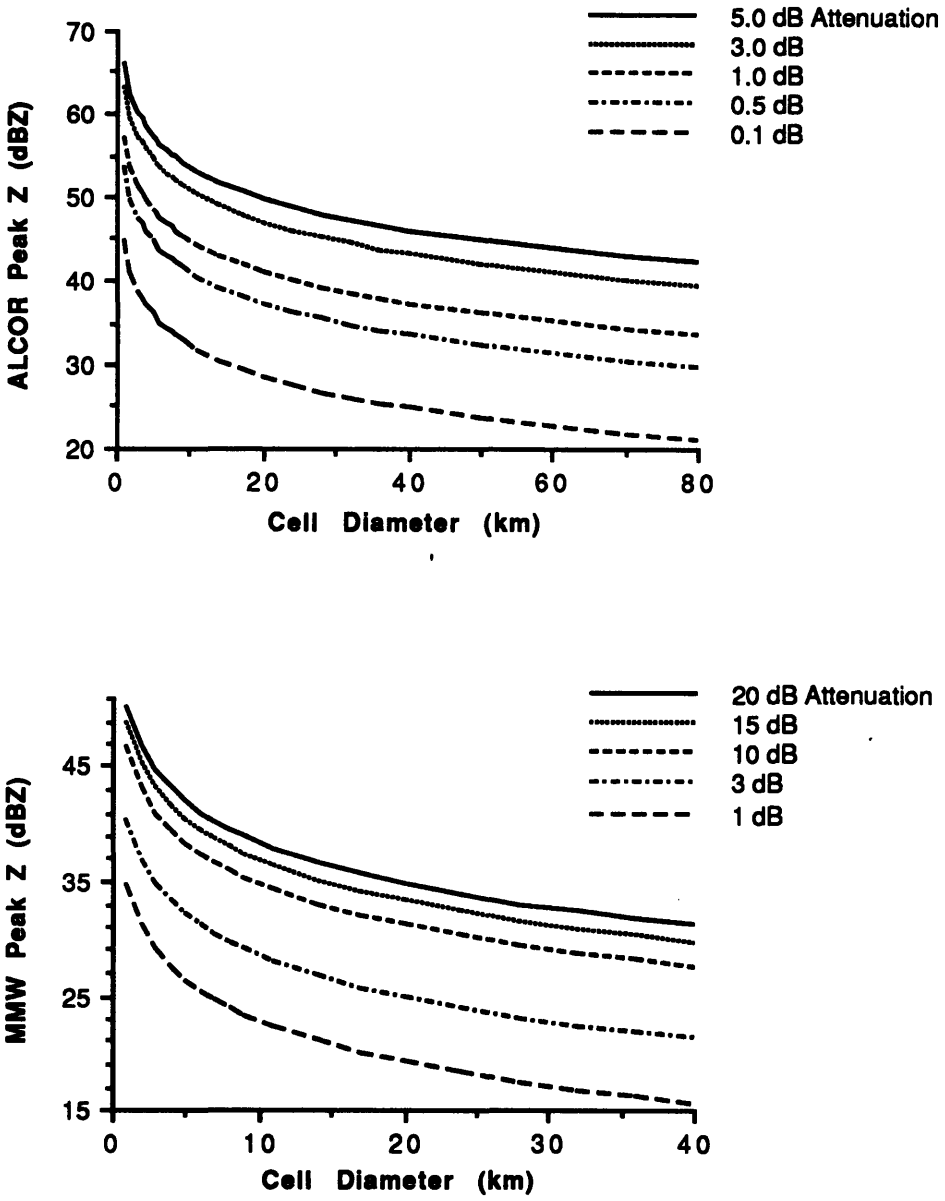

Figure 5.10 Peak reflectivity versus cell diameter for various values of total attenuation for ALCOR and MMW, for the Gaussian distribution of reflectivity levels in weather cell model #2.

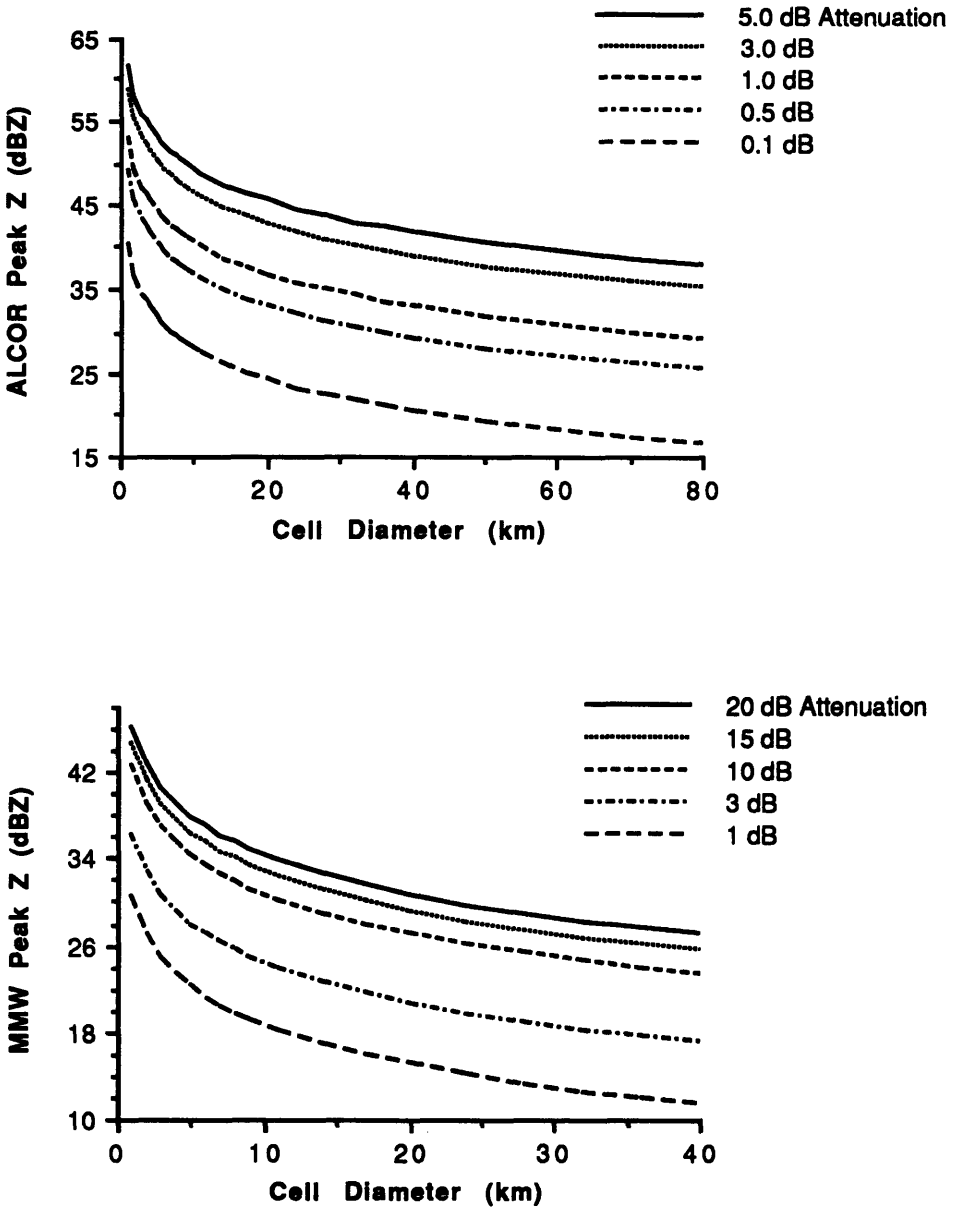

Figure 5.11 Peak reflectivity versus cell diameter for various values of total attenuation for ALCOR and MMW, for the constant reflectivity levels of weather cell model #1.

6. Summary

The succeeding sections present an overview of the proposed attenuation algorithm, which was developed, followed by a summary of the issues involved in the implementation of the algorithm.

6.1. The Proposed Algorithm

Various relations between meteorological phenomena and radar measurements of weather, were evaluated for use in the proposed algorithm.

- An algorithm was developed, which corrects for attenuation of RCS measurements due to weather, using radar reflectivity measurements of the weather of interest.
- The author recommends the use of the Wexler and Atlas Z-R relations, based on their modified Marshall-Palmer droplet-size distributions, in the proposed algorithm (section 4.5). However, the Blanchard Z-R relation also performed acceptably in the analysis of the experimental data, and either Z-R relation would be adequate for use in the algorithm.
- The Waldteufel k-R relations are also recommended over the Wexler and Atlas k-R relations, although either set of relations would also perform adequately in the algorithm.
- For low frequency radar systems such as ALCOR, for which Rayleigh scattering predominates, the variation of temperature with altitude must be taken into account in the attenuation algorithm. For radar frequencies above about 18 GHz however (such as MMW), one may assume that the attenuation is constant for temperatures in the range of 0 to 40°C.

- The performance of the proposed algorithm in analyzing the experimental data was very promising. However, due to experimental constraints, only a limited number of test cases were available. Therefore, these results do not give conclusive proof of the validity of the algorithm, and further experimental analysis is strongly recommended.

6.2. Implementation of the Algorithm

Several issues affecting the implementation of the algorithm were addressed in detail, as well as the possibility of establishing meaningful criteria for aborting missions due to weather at the KREMS facility.

- Scanning procedures were recommended for range scans made immediately following, or shortly after, RCS measurements of reentry vehicles or other targets.

- A procedure for predicting the arrival of weather cells within the test area, based on knowledge of the prevailing winds, was also presented. This was based on the consistent nature of the movement of weather cells around the Kwajalein Atoll.

- A determination of the time scales of weather cell dynamics was not possible, but further analysis in this area is recommended.

- Various criteria for determining the altitude, above which the weather attenuation may be neglected, were evaluated. A direct identification of the bright-band is best, but a cutoff altitude at approximately 500 meters below the altitude of the 0°C isotherm is acceptable.

- A method was presented, for determining the necessity of mission aborts, based on PPI scans of the weather around the KREMS facility.

Appendix A: Attenuation by Atmospheric Gases

Molecules of water vapour have permanent electric dipole moments, and those of oxygen have permanent magnetic dipole moments. Hence, any electromagnetic wave transmitted through the atmosphere, interacts with these molecules and causes them to vibrate, imparting energy to them. This energy is eventually re-radiated, but in every direction, so that the net effect is a reduction in the energy of the directed wave. Figure A1, from Lhermitte (1987), is a plot of one way atmospheric attenuation for various levels of specific humidity. This graph demonstrates that even at relatively low humidity levels, the attenuation due to atmospheric gases is considerable for frequencies above about 10 GHz.

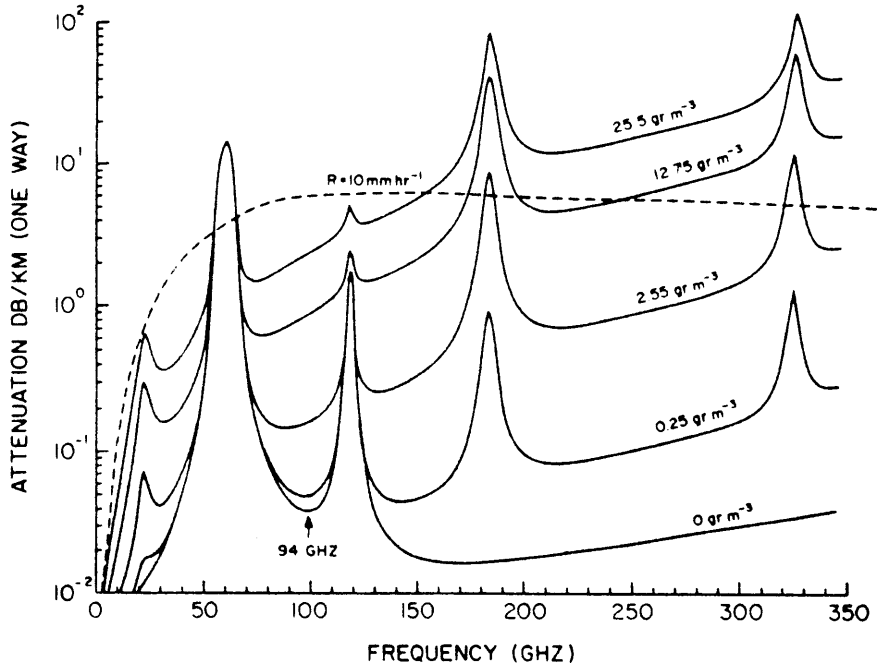

Figure A1 **Absorption spectrum for atmospheric gases at the ground for various humidity conditions indicated by the specific humidity values. The absorption due to a 10 mm/hr rainfall is also shown.**
From Lhermitte (1987).

Appendix B: Attenuation by Clouds

Cloud particles are small enough (diameters ≤ 100 μ) to be considered Rayleigh scatterers for centimeter and millimeter wavelengths, so that equation (3.6) may be used to determine the attenuation cross-section of these particles. In this case, the attenuation rate of equation (3.10) becomes

$$k = 0.4343 \frac{\pi^2}{\lambda} \mathrm{Im}(-K) \sum_1 D^3 \qquad \text{(B.1a)}$$

$$= 0.4343 \frac{\pi^2}{\lambda} \frac{M}{\rho} \mathrm{Im}(-K) \qquad \text{(B.1b)}$$

Gunn and East (1954) used this equation to calculate attenuation rates for water and ice clouds, as a function of liquid water content. The results for various wavelengths are listed below in Table B1.

Temperature (°C)		k/M (dB km^{-1}/gm m^{-3}) at indicated wavelengths			
		0.9 cm	1.8 cm	3.2 cm	5.7 cm
Water	20	6.47 x 10^{-1}	1.28 x 10^{-1}	4.83 x 10^{-2}	1.36 x 10^{-2}
	10	6.81 x 10^{-1}	1.79 x 10^{-1}	6.30 x 10^{-2}	1.96 x 10^{-2}
	0	9.9 x 10^{-1}	2.67 x 10^{-1}	8.58 x 10^{-2}	2.72 x 10^{-2}
	-8	12.5 x 10^{-1}	*3.4 x 10^{-1}	*11.2 x 10^{-2}	*3.4 x 10^{-2}
Ice	0	8.74 x 10^{-3}	4.36 x 10^{-3}	24.6 x 10^{-4}	13.8 x 10^{-4}
	-10	2.93 x 10^{-3}	1.46 x 10^{-3}	8.19 x 10^{-4}	4.60 x 10^{-4}
	-20	2.00 x 10^{-3}	1.00 x 10^{-3}	5.63 x 10^{-4}	3.16 x 10^{-4}

* Extrapolated values.
SOURCE: Gunn and East (1954).

Table B1 One-way attenuation rate, k in dB km^{-1}, per unit liquid water content, M in gm m^{-3}, for ice and water clouds, assuming Rayleigh scattering.

Appendix C: Effects of Temperature on Attenuation Rate

The following table of attenuation rates was prepared by Waldteufel (1973) for Mie scattering, using the Marshall-Palmer droplet-size distribution.

Wavelength (cm)		One-way Attenuation Rate (dB km^{-1})			
		0°C	10	18	40
0.3	R = 1	1.16	1.20	1.21	1.20
	10	0.704	0.714	0.714	0.702
	100	0.383	0.384	0.384	0.375
0.5	1	0.628	0.631	0.629	0.625
	10	0.517	0.515	0.511	0.498
	100	0.343	0.340	0.336	0.325
0.75	1	0.287	0.284	0.285	0.298
	10	0.309	0.306	0.303	0.303
	100	0.265	0.260	0.256	0.256
1.0	1	0.150	0.150	0.153	0.167
	10	0.184	0.184	0.185	0.192
	100	0.193	0.189	0.187	0.186
1.5	1	0.0596	0.0596	0.0608	0.0640
	10	0.0779	0.0808	0.0839	0.0833
	100	0.101	0.101	0.103	0.108
2.0	1	0.0309	0.0298	0.0292	0.0265
	10	0.0438	0.0459	0.0459	0.0500
	100	0.0573	0.0600	0.0624	0.0684
3.0	1	0.0115	0.0101	0.0089	0.0061
	10	0.0160	0.0161	0.0159	0.0142
	100	0.0251	0.0273	0.0287	0.0309
6.0	1	0.00218	0.00161	0.00131	0.00080
	10	0.00231	0.00177	0.00144	0.00086
	100	0.00372	0.00315	0.00268	0.00159

SOURCE: Waldteufel (1973).

Table C1 Influence of temperature on the attenuation rate for the Marshall-Palmer droplet-size distribution, for different values of wavelength and rainfall rate. Calculated by Waldteufel (1973).

Appendix D: Derivation of Im(-K) Values for ALCOR

The Im(-K) values for ALCOR (λ = 5.3 cm) were calculated using the following expression for m, the complex index of refraction, developed by Lane and Saxton (1952).

$$m^2 = \varepsilon_o + \frac{\varepsilon_s - \varepsilon_o}{1 + j\omega\tau} \qquad (D.1)$$

where ε_s = the static dielectric constant,

ε_o = the optical dielectric constant (Lane and Saxton suggest a value of 4.9),

ω = $2\pi f$, where f is the frequency

and τ = the relaxation time (from Debye 1929).

From the definition of K given in equation (3.7), the resulting expression for Im(-K) was

$$\text{Im}(-K) = \frac{3\omega\tau\,(\varepsilon_s - 4.9)}{(\varepsilon_s + 2)^2 + 47.61(\omega\tau)^2} \qquad (D.2)$$

Values for ε_s and τ at -8, 0, 10, 20, and 30°C were taken from plots in Waldteufel (1973), and are listed below in Table C1.

Temperature (°C)	τ	ε_s	Im(-K)
30	7.3×10^{-12}	76.7	0.00903
20	9.65×10^{-12}	80.4	0.01145
10	1.3×10^{-12}	84.0	0.01482
0	1.85×10^{-11}	88.4	0.02013
-8	2.49×10^{-11}	92.4	0.02599

Table D1 Im(-K) values for ALCOR (λ = 5.3 cm) over the temperature range of -8°C to 30°C.

Appendix E: Altitude Derivation for RHI Scans

For both RHI scans shown in Figure 4.1, the vertical grid is printed at 4 km intervals. However, the horizontal (ground range) grid is printed at intervals of 32 km for experiment #1, and 8 km for experiment #2. For a short range, as in scan #2 (the scan for experiment #2) the curvature of the ground is insignificant, and the altitude, h in km, can be found directly from the tangent of the elevation angle.

$$h = s \tan(\alpha) \tag{E.1}$$

where s = the ground range in km,

and α = the elevation angle in degrees.

For a longer range, such as in scan #1 (the scan for experiment #1) the curvature is very pronounced, and must be taken into account. In this case the altitude, h, is the sum of two heights, h_1 and h_2, where h_1 is the altitude, at range s, of a line which is tangent to the Earth at the radar, and h_2 is the height of the elevation path above that line, as shown in Figure E1.

The value of h_1 (in km) can be calculated from the average radius of the Earth, 6370 km, using the Pythagoras Theorem.

$$h_1 = \sqrt{d^2 + 6370^2} - 6370 \tag{E.2}$$

where d is the distance of the radar from the altitude line (see Figure E1), and is given by

$$d = \frac{6370 \sin(\beta)}{\sin(90 - \beta)} \tag{E.3}$$

and

$$\beta \equiv \frac{180}{\pi} \times \frac{s}{6370} \tag{E.4}$$

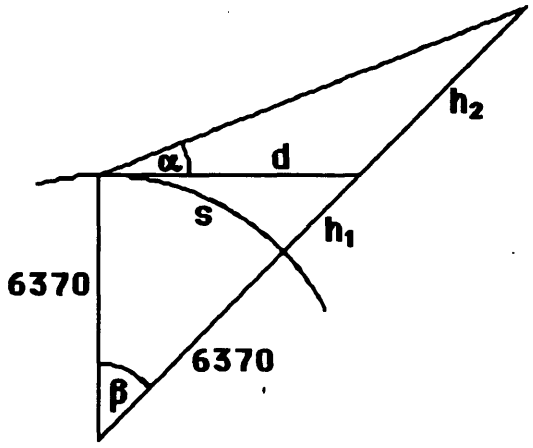

Figure E1 Effect of Earth's curvature on altitude derivation.

The value of h_2 (in km) can then be determined from these parameters, and the law of sines for a triangle.

$$h_2 = \frac{d \sin(\alpha)}{\sin(90 - \alpha - \beta)} \qquad \text{(E.5)}$$

and the altitude is simply

$$h = h_1 + h_2 \qquad \text{(E.6)}$$

Appendix F: Results of Time Scale Analysis for ALCOR

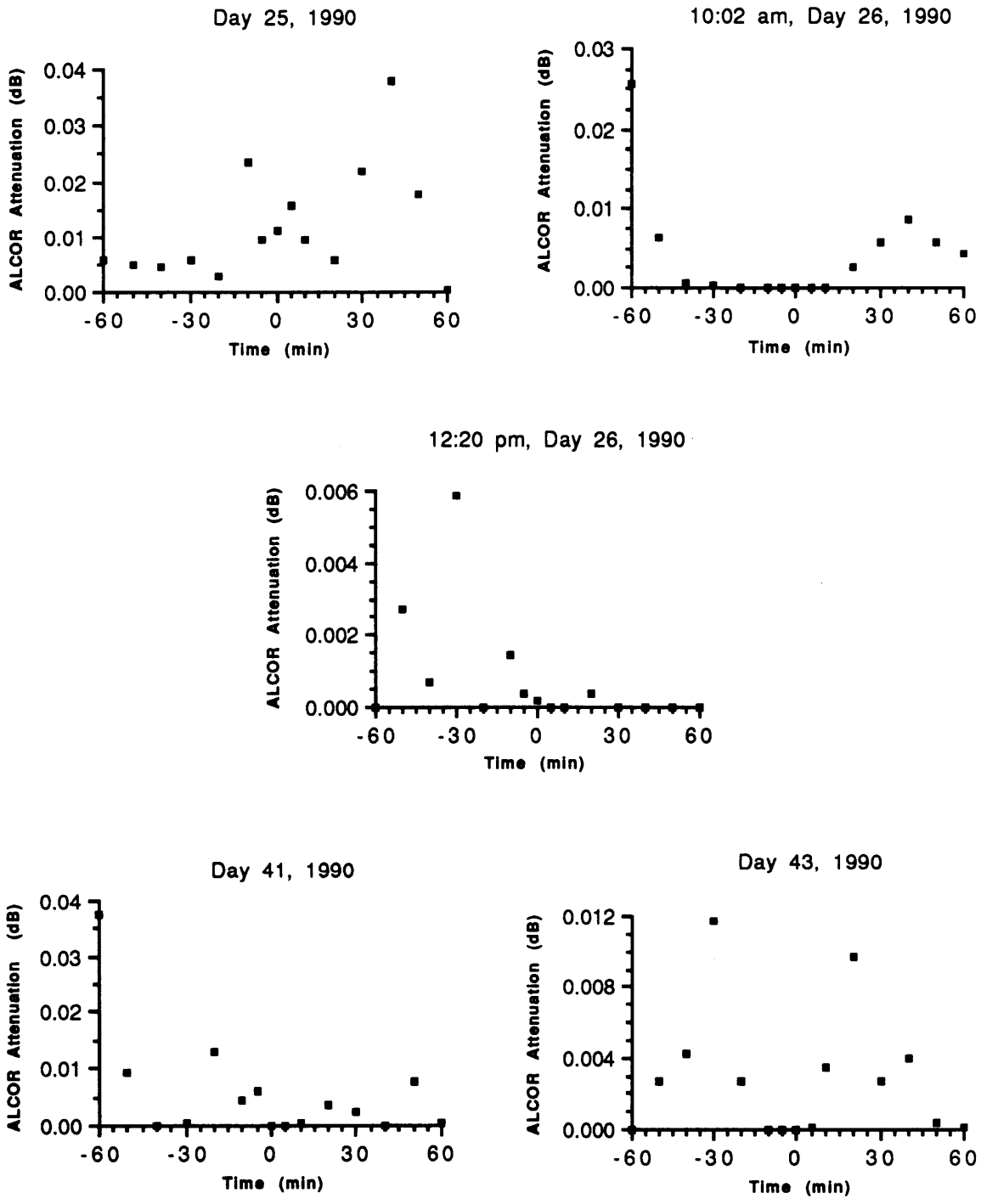

Figure F1 **Plots of calculated attenuation along the 45° azimuth on four different days, from the NASA TRMM data.**

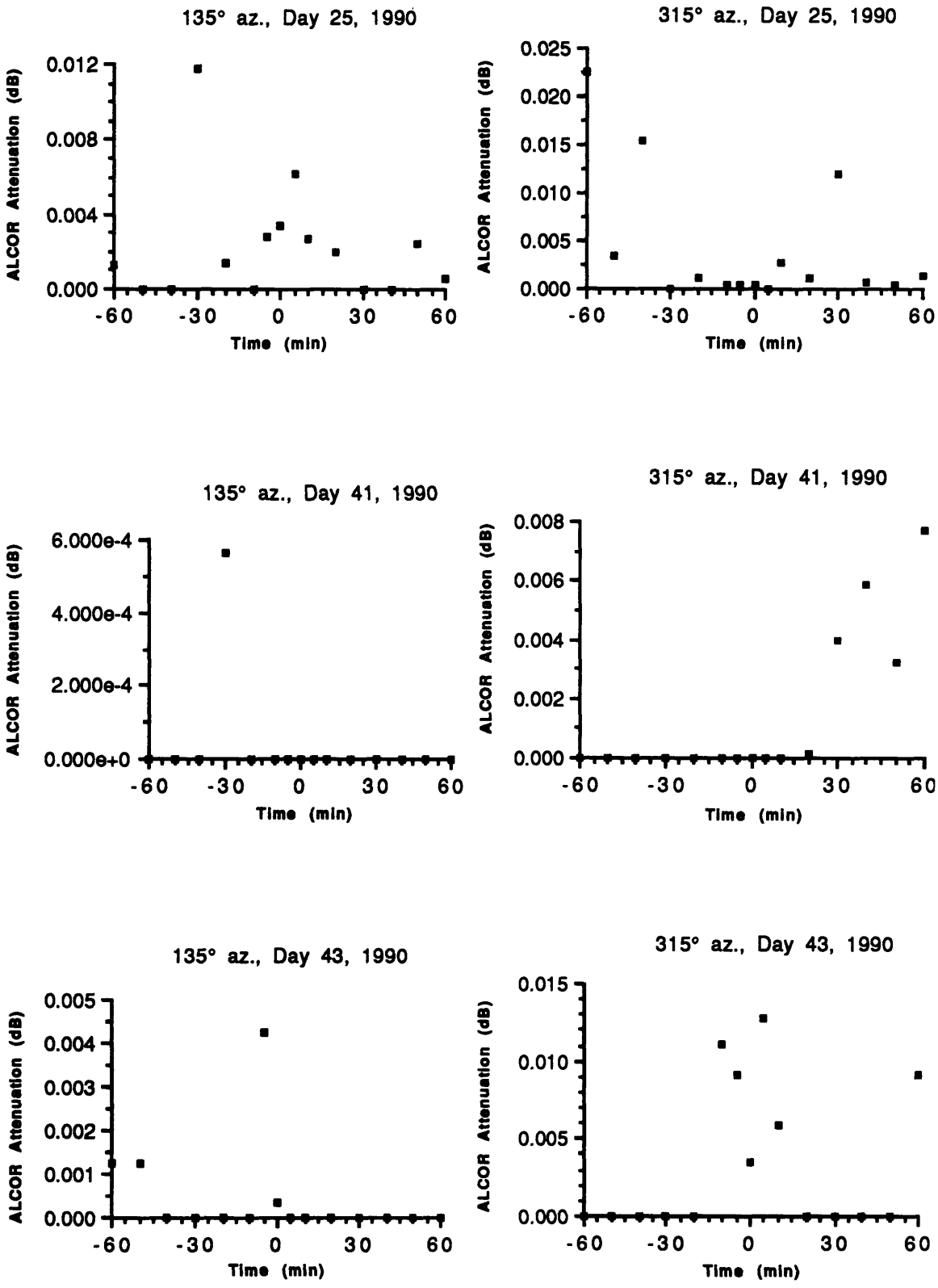

Figure F2 **Plots of calculated attenuation along the 135° and 315° azimuths on three different days, from the NASA TRMM data.**

Appendix G: Abort Criteria Relations

For two-way attenuation rate, k_2 in dB km^{-1}, as a function of the reflectivity factor, Z in mm^6 m^{-3}, expressed in the form

$$k_2 = a Z^b \tag{G.1}$$

and the Gaussian-like distribution of reflectivity levels, as given in section 5.4,

$$Z = Z_o e^{-\pi(x Z_o / C)^2} \tag{G.2}$$

the total two-way attenuation, A_2 in dB, is given by

$$A_2 = \int_{-r}^{r} k_2 \, dx = \int_{-r}^{r} a Z_o^b e^{-\pi(x Z_o / C)^2} dx \tag{G.3}$$

where r = the radius of the weather cell in km,

x = the distance from the center of the cell in km,

Z_o = the peak reflectivity in dBZ,

and C = a constant which scales the integral to any value, not necessarily unity.

This integral may be solved by using the substitution

$$y = \frac{x Z_o}{C} \sqrt{b \pi} \tag{G.4}$$

so that equation (F.3) becomes

$$A_2 = \frac{2 C a Z_o^b}{Z_o \sqrt{b \pi}} \int_0^{\frac{r Z_o \sqrt{b \pi}}{C}} e^{-y^2} \, dy \tag{G.5a}$$

$$= \frac{C a Z_o^b}{Z_o \sqrt{b}} \operatorname{erf}\left(\frac{r Z_o \sqrt{b \pi}}{C}\right) \tag{G.5b}$$

Then, by assuming the intensity at the cell perimeter (x = r) is 20 dB below the level at the center, equation (G.2) becomes

$$Z = Z_o e^{-\pi(r Z_o/C)^2} = \frac{Z_o}{100} \tag{G.6}$$

which results in the expression

$$\frac{r Z_o}{C} = \sqrt{\frac{\ln(10^{-2})}{-\pi}} \approx 1.2107 \tag{G.7}$$

Substituting this into equation (F.4b), the total two-way attenuation becomes

$$A_2 = \frac{a d Z_o^b}{2.4214 \sqrt{b}} \operatorname{erf}(1.2107 \sqrt{b \pi}) \tag{G.8}$$

where $d = 2r$ is the cell diameter.

From the NASA TRMM data, it was apparent that reflectivity levels above 42 dBZ are extremely rare around the Kwajalein Atoll. Therefore, a hybrid of the two-way attenuation rates which are valid for reflectivity levels of up to 42 dBZ, was used. For MMW, the hybrid attenuation rate in dB km^{-1}, derived from equations (3.23a,b), and (3.27a,b), was expressed as a function of Z in $mm^6 m^{-3}$ as follows.

$$\bar{k}_{2M} = 2.85 \times 10^{-3} Z^{0.83} \tag{G.9}$$

The hybrid attenuation rate for ALCOR was derived from equation (3.22) and equations (3.26a to c), for this range of reflectivity values. Since temperature effects were ignored in this simplified model (18°C temperature was assumed throughout), an under-estimation of the attenuation values for ALCOR was expected. Therefore, the hybrid attenuation rate was increased by 25%, which is typical of the change from constant temperature at 18°C to variable temperature, as mentioned in section 4.4.3. This was again

increased by 25%, in order to account for undervalued Z_e measurements in the weather scan, as discussed in section 5.3.1. The corresponding average attenuation rate for ALCOR in dB km^{-1} was as follows.

$$\bar{k}_{2A} = 5.77 \times 10^{-5} Z^{0.8} \qquad \text{(G.10)}$$

From equations (G.9) and (G.10), the values of b for ALCOR and MMW are 0.8 and 0.83 respectively, so that the error function term[1] of equation (G.8) is approximately 0.99 for each. Therefore, for both ALCOR and MMW, equation (G.8) can be written as

$$A_2 = \frac{0.99\, a\, d\, Z_o^b}{2.4214\, \sqrt{b}} \qquad \text{(G.11)}$$

[1] Error function values can be found in a mathematical handbook such as the "CRC Handbook of Tables for Probability and Statistics," William H. Beyer, Editor, The Chemical Rubber Co., 1966.

References

Anderson, L. J., Day, J. P., Freres, C. H., and Stokes, A. P. D.	1947	"Attenuation of 1.25 cm Radiation Through Rain," Proceedings of the Institute of Radio Engineers, Vol. 35, Page 351.
Austin, Pauline M.	1964	"Observations of Attenuation of 3 cm. Radiation by Precipitation," World Conference on Radio Meteorology.
Aydin, K., Zhao, Y.A., and Seliga, T. A.	1989	"Rain-Induced Attenuation Effects on C-Band Dual-Polarization Meteorological Radars," IEEE Transactions on Geoscience and Remote Sensing, Vol. 27, No.1.
Basharinov and Kutuza.	1968	"Radio Emission and Absorption of Cloudy Atmosphere in mm and cm Ranges," Transactions of Third All-Union Conference on Radar Meteorology.
Battan, L. J.	1973	"Radar Observation of the Atmosphere," University of Chicago Press.
Bentley, Wilson A.	1904	"Studies of Raindrops and Raindrop Phenomena," Mon. Wea. Rev., Vol. 32, Pages 450-456.
Blanchard, D. C.	1953	"Raindrop Size Distribution in Hawaiian Rains," Journal of Meteorology, Vol. 10.
Debye, P.	1929	"Polar Molecules,"The Chemical Catalogue Co. Inc., New York.
Deirmendjian, D.	1964	"Complete Scattering Parameters of Polydispersed Hydrometeors in the $\lambda 0.1$ to $\lambda 10$ cm Range," World Conference on Radio Meteorology.
Dicke, R. H., Beringer, R., Kyhl, R. L., and Vane, A. B.	1946	"Atmospheric Absorption Measurements with a Microwave Radiometer," Physical Review, Vol. 70, Nos. 5 & 6.

Fuhs, Allen E.		"Radar Cross Section Lectures," Published by AIAA.
Gunn, K. L. S., and East, T. W. R.	1954	"The Microwave Properties of Precipitation Particles," Quarterly Journal of the Royal Meteorological Society, Vol. 80, Pages 522-545.
Haddock, F. T.	1948	"Scattering and Attenuation of Microwave Radiation through Rain," Naval Research Laboratory, Washington D. C. (unpublished manuscript).
Herman, B. M., Browning, S. R., and Battan, L. J.	1961	"Tables of the Radar Cross Sections of Water Spheres," Technical Report No. 9, Institute of Atmospheric Physics, University of Arizona.
Herman, Benjamin M.	1964	"The Effects of Multiple Scattering on Radar Back-scattering," World Conference on Radio Meteorology.
Jameson, A. R.	1989	"Theoretical Analysis and Meteorological Interpretation of the Role of Raindrop Shape on Microwave Attenuation and Propagation Phase Shifts: Implication for the Radar Measurement of Rain," Journal of Atmospheric and Oceanic Technology, Vol. 6, No.1.
Kutuza, B. G.	1968	"Experimental Studies of Attenuation and radio Emission of Rain in the SHF Range," Transactions of Third All-Union Conference on Radar Meteorology.
Lane, J. A., and Saxton, J. A.	1952	"Dielectric Dispersion in Pure Polar Liquids at Very High Radio Frequencies," Proc. Roy. Soc. A, Vol. 213.
Laws, J. Otis, and Parsons, Donald A.	1943	"The Relation of Raindrop-size to Intensity," American Geophysical Union Transactions, Vol. 24.

Leeper, John L.	1986	"Three Dimensional Weather Scan," Letter to Major Dave Helma, 30 October.
Lhermitte, Roger	1986	"Cloud and Precipitation Observation with 94 GHZ Doppler Radar," American Meteorological Society, 23rd Conference on Radar Meteorology and the Conference on Cloud Physics, September 22 - 26.
Lhermitte, Roger	1987a	"A 94-GHZ Doppler Radar for Cloud Observations," Journal of Atmospheric and Oceanic Technology, Vol. 4, No. 1.
Lhermitte, Roger	1987b	"Small Cumuli Observed with a 3 mm Wavelength Doppler Radar," Geophysical Research Letters, Vol. 14, No. 7, Pages 707-710, July.
Lhermitte, Roger	1988	"Observation of Rain at Vertical Incidence with a 94 GHZ Doppler Radar: An Insight on Mie Scattering," Geophysical Research Letters, Vol. 15, No. 10, Pages 1125-1128.
Lhermitte, Roger	1990a	"Attenuation and Scattering of Millimeter Wavelength Radiation by Clouds and Precipitation," Journal of Atmospheric and Oceanic Technology, Vol. 7, No. 3, June.
Lhermitte, Roger	1990b	"Observations of Stratiform Rain with 94 GHz and Ka-Band Radars,"Technical Report No. GL-TR-90-0004 for the Geophysics Laboratory, Air Force Systems Command, United States Air Force, Hanscom Air Force Base, Massachusetts, May 23.
Marshall, J. S., and Palmer, W. McK.	1948	"The Distribution of Raindrops with Size," Journal of Meteorology, Vol. 5.
May, E. G.	1988	"HARP Sphere Drop in Weather," Lincoln Laboratory Internal Memorandum, 24 October.

Mueller, E. A., and Jones, D. M. A.	1960	"Drop-size Distributions in Florida," Proceedings of the Eighth Weather Radar Conference, Boston, American Meteorological Society, Pages 299-305.
Mueller, E. A.	1964	"A Study of the Radar Precipitation Attenuation as Deduced from Drop Size Distributions," World Conference on Radio Meteorology.
Pani, Eric A., and Jurica, Gerald M.	1989	"A Z-R Relation for Summertime Convective Clouds over West Texas," Journal of Applied Meteorology, Vol. 28, No. 10.
Pavlov, N. F.	1968	"Attenuation of Precipitation Reflections in Radars with Linear Polarization," Transactions of Third All-Union Conference on Radar Meteorology.
Pearson, K. E., and Culberson, B. J.	1986	"Program MOIST II," Lincoln Laboratory Memorandum, 10 February.
Pearson, K. E.	1985a	"Four Frequency Weather Comparisons on Ice Hydrometeors," Lincoln Laboratory Internal Memorandum, 23 July.
Pearson, K. E.	1985b	"MOIST II - A Proposal," Lincoln Laboratory Memorandum, 23 December.
Pearson, K. E.	1986a	"The Origins of the Reflectivity Factor (z) versus Liquid Water Content (M) Relationships Currently in use at KREMS," Lincoln Laboratory Internal Memorandum, 13 January.
Pearson, K. E.	1986b	"Two Examples of Liquid Water Content Calculations by the MOIST Program," Lincoln Laboratory Memorandum, 11 February.
Pearson, K. E.	1986c	"New Z-M Relationships For Use in the MOIST I & II Programs," Lincoln Laboratory Internal Memorandum, 11 March.

Pearson, K. E.	1986d	"MMW 35GHz RCS to KDC," Lincoln Laboratory Internal Memorandum, 18 April.
Pearson, K. E.	1986e	"ALCOR/MMW NB1 Weather Comparisons and the SENT Mission," Lincoln Laboratory Internal Memorandum, 23 September.
RCA Aerospace and Defense Electronic Systems Department, Moorestown, N.J.	1988	"KDC/KCC Weather Sampling Capability", Doc. No. 208, Systems Manual prepared for the United States Army Strategic Defense Command under Prime Army Contract No. DASG60-86-C-0002, 22 March.
Stephens, J. J.	1961	"Radar Cross-Sections for Water and Ice Spheres," Journal of Meteorology, Vol. 18, Pages 348-359.
Waldteufel, P.	1973	"Attenuation des Ondes Hyperfrequences par la Pluie: Une Mise au Point," Ann. Tellecomm., Vol. 28, Pages 255-272.
Wexler, R. and Atlas, D.	1963	"Radar Reflectivity and Attenuation of Rain," Journal of Applied Meteorology, Vol. 2.
Wexler, R.	1984	"Rain Intensities by Radar," Journal of Meteorology, Vol. 5.
Yokoyama, Tatsuo	1985	"Two-Wavelength (0.86 cm and 3.2 cm) Radar Observation of Microphysical Process in Stratiform Precipitation - Part I. Attenuation of Radar Wave Due to Precipitation Particles and Correction Method," Journal of the Meteorological Society of Japan, Vol. 63, No. 6.